Empirical Stochastic Modeling of Multipath Polarizations in Indoor Propagation Scenarios

Xuefeng Yin, *Member, IEEE*, Yongyu He, *Student Member, IEEE*, Cen Ling, *Student Member, IEEE*, Li Tian, *Member, IEEE*, and Xiang Cheng, *Senior Member, IEEE*

***Abstract*—In this contribution, a stochastic modeling approach is proposed for characterizing the polarization status of multipath components (MPCs) in propagation channels. The 2×2 polarization matrix of each MPC is represented by the geometrical parameters of two ellipses, i.e., the ovality, tilt angle, and size of each ellipse, as well as the rotating direction of electric field intensity along the ellipse. The statistics of these parameters including correlation behaviors among them extracted from measurement data constitute the stochastic polarization model for the propagation scenario of interest. Analytical expressions are presented for the transformation from the ellipse parameters to the 2×2 polarization matrix, and vice versa. Comparing with conventional polarization models addressing merely the cross-polarization ratios, the new model provides a more complete description for the per-path polarizations in terms of the power imbalance, tilting, and polarization spread. Furthermore, based on multiple-input multiple-output channel measurement data collected with 100-MHz bandwidth and at the center frequency of 5.25 GHz, stochastic polarization models of the proposed structure are extracted for five indoor scenarios. These models are complementary to the existing geometry-based stochastic channel models for generating realistic polarization matrices for MPCs.**

***Index Terms*—Geometry-based stochastic channel model, high-resolution parameter estimation, polarization ellipse, wideband propagation channel.**

I. Introduction

In wireless communication systems, multiple-input multiple-output (MIMO) techniques have been extensively applied in order to achieve significant spectrum efficiency and communication reliability by means of spatial multiplexing, beamforming, or diversity [1], [2]. Theoretically, the capacity of an MIMO system per unit power and bandwidth grows linearly with respect to the number of elements in the antenna arrays in rich-scattering environments [3]. Empirically, the MIMO performance is constrained by both the size of the antenna array that can be accommodated at a base station or in a user equipment and the limited number of uncorrelated spatial channels existing in real environments. Polarization in different orientations can be used as a new resource to increase the number of uncorrelated channels without enlarging array size [4], [5]. Recently, various dual- and tri-polarized transmission techniques have been proposed and studied [6]–[11]. By appropriately selecting polarization transmission techniques, the capacity of MIMO systems can be enhanced significantly [12]–[14].

Accurate description of the behavior of realistic propagation channels is essential for designing and evaluating wireless communication techniques or systems. Conventional research on channel polarimetric properties can be categorized into two classes: 1) narrowband studies on channel coefficients observed between linearly polarized antennas at the transmitter and at the receiver, respectively, and 2) wideband studies on the statistics of polarizations for multipath or cluster of paths. Examples of narrowband channel polarization modeling are given in [15], where the stochastic models for the copolarization ratio (CPR), cross-polarization ratio (XPR), and spatial correlations thereof were established for dual-polarized Rayleigh and Ricean fading channels based on the measurements in various propagation scenarios. Another example shown in [16] presents a closed-form representation of the cross-polarization discrimination (XPD) of a narrowband channel as a function of antenna orientations which matches nicely with measurement results. Besides modeling directly the co- and cross-polarization properties, the entries of a narrowband channel polarization matrix can also be transformed into ellipses. The temporal autocorrelation behaviors of the parameters characterizing these ellipses were studied in [17].

The wideband studies of polarizations focus on the characteristics of multipath components (MPCs). MPCs' parameters estimated by using the space-alternating generalized expectation-maximization (SAGE) algorithm from outdoor measurement data have illustrated a significant variability of the polarization ellipses for individual paths [18], [19]. The statistics of the XPD or XPR per path has been modeled as functions of geometrical parameters of MPCs in [20]–[22]. Such per-path-XPD descriptions have been included in the stochastic channel models in many standards, such as 3GPP spatial channel models (SCMs) [23], the wireless world initiative new radio (WINNER) SCM-enhanced (SCME) [24], [25], and the

Manuscript received September 30, 2014; revised September 16, 2015; accepted September 29, 2015. Date of publication October 05, 2015; date of current version November 25, 2015. This work was jointly supported by the general project (61471268) of the National Natural Science Foundation of China (NSFC), the NSFC Key Program (61331009), and the Key program (2016ZX03001015) of National Science and Technology Major Project of the Ministry of Science and Technology of China. *(Corresponding author: Xuefeng Yin.)*

X. Yin and C. Ling are with the College of Electronics and Information Engineering, Tongji University, 201804 Shanghai, China (e-mail: yinxuefeng@tongji.edu.cn; 1410048@tongji.edu.cn).

Y. He is with the College of Physics Science and Engineering, Tongji University, 200092 Shanghai, China (e-mail: 1989heyongyu@tongji.edu.cn).

L. Tian was with the College of Electronics and Information Engineering, Tongji University, 201804 Shanghai, China. He is now with ZTE Corporation, 201203 Shanghai, China (e-mail: tian.li150@zte.com.cn).

X. Cheng is with the School of Electronics Engineering and Computer Science, Peking University, 100871 Beijing, China, and also with Qingdao Academy of Intelligent Industries, 266109 Qingdao, China (e-mail: xiangcheng@pku.edu.cn).

Color versions of one or more of the figures in this paper are available online at http://ieeexplore.ieee.org.

Digital Object Identifier 10.1109/TAP.2015.2486798

IMT-advanced models [26]. The polarizations of individual clusters represented by a 2×2 polarization matrix are generated based on the statistics of XPRs specified in these models.

Recent studies have shown that the MPCs' polarizations can be easily changed by both the coherence properties of the paths involved in a cluster [27], [28] and the orientation of the user equipment with respect to the transmitter [29]. To describe these variations more efficiently, new parameters have been introduced, such as the linear polarization angle (LPA) calculated as the arc-tangent of the received horizontal to vertical polarization power ratio [30], and the polarization spread defined to be the second-central-moment of the MPCs' LPAs in a channel. Nevertheless, these new parameters are still insufficient to characterize a 2×2 complex polarization completely. Some important properties, such as the phase differences among the matrix entries and the power imbalance of polarized channels, are either neglected or not thoroughly investigated so far. Since the polarizations have been considered as an additional degree of freedom supplementary to MIMO techniques, it is necessary to build empirical stochastic models which describe the characteristics of parameters that uniquely determine the polarizations for individual MPCs.

In this contribution, inspired by the analysis of polarization ellipses in [18], [19], and [30], we propose a polarimetric modeling approach which utilizes geometry-based parameters to describe per-path polarizations. More specifically, the 2×2 complex polarization matrix is transformed to eight geometrical parameters, which uniquely determine the two elliptical trajectories along with the electric field intensity vectors oscillate. The parameters of each trajectory include the size, the ovality, and the tilt of the ellipse, as well as the rotation orientation with respect to the propagation direction. The statistics of these parameters constitute a stochastic polarization model. The advantages of modeling the parameters of polarization ellipses instead of XPRs lie on the fact that the polarization of a channel is completely described by these parameters, which allows analyzing the system performance with respect to the statistics of the parameters. Furthermore, we also established empirical stochastic polarization models for indoor environments based on the measurement data collected by using the wideband channel sounder—PROPsound [31]. The statistical differences of these ellipse parameters in various environments demonstrate the possibility of distinguishing polarizations precisely among multiple refined environments. These models can be used as supplementaries to the existing SCMs or SCMEs for channel simulations in dual-polarization scenarios.

This paper is organized as follows. In Section II, the ellipses' parameters characterizing the polarization matrix of a path are defined. The stochastic modeling approach is proposed. The analytical expressions of the entries of polarization matrix in terms of these ellipses' parameters are derived. In Section III, the wideband channel measurement campaign is described, and the stochastic models extracted for five indoor scenarios are elaborated. In Section IV, the effect of using the established models to simulate the distributions of polarized path capacities and the ratio of singular values of polarization matrix is investigated. Finally, concluding remarks are given in Section V.

II. Geometry-Based Approach for Polarization Matrix Characterization

A. Polarization Matrix of Propagation Path Revisited

Let us consider a MIMO system with M_1 antennas at the transmitter (Tx) and M_2 antennas at the receiver (Rx). The propagation channel between the Tx and the Rx consists of L specular paths each characterized by delay, direction (i.e. azimuth and elevation) of departure (DoD), direction of arrival (DoA), Doppler frequency, and polarization matrix [32]. Under the far-field and small-scale characterization assumptions, the baseband representation of the signal component contributed by the ℓth path to the output of the Rx antennas can be written as [18], [33], [34]

$$\boldsymbol{s}(t;\boldsymbol{\psi}_\ell) = \exp\{j2\pi\upsilon_\ell t\}\, \boldsymbol{C}_{\mathrm{Rx}}(\boldsymbol{\Omega}_{\mathrm{Rx},\ell}) \boldsymbol{A}_\ell \boldsymbol{C}_{\mathrm{Tx}}(\boldsymbol{\Omega}_{\mathrm{Tx},\ell})^{\mathrm{T}} \boldsymbol{u}(t-\tau_\ell) \tag{1}$$

where $\boldsymbol{u}(t) = [u_1(t), \ldots, u_{M_1}(t)]^{\mathrm{T}}$ with $(\cdot)^{\mathrm{T}}$ being the transpose operation denotes the baseband signals at the input of the Tx array, and

$$\boldsymbol{C}_{\mathrm{Tx}}(\boldsymbol{\Omega}_{\mathrm{Tx},\ell}) = [\boldsymbol{c}_{\mathrm{Tx},\theta}(\boldsymbol{\Omega}_{\mathrm{Tx},\ell})\ \boldsymbol{c}_{\mathrm{Tx},\phi}(\boldsymbol{\Omega}_{\mathrm{Tx},\ell})] \in \mathcal{C}^{M_1 \times 2} \tag{2}$$

$$\boldsymbol{C}_{\mathrm{Rx}}(\boldsymbol{\Omega}_{\mathrm{Rx},\ell}) = [\boldsymbol{c}_{\mathrm{Rx},\theta}(\boldsymbol{\Omega}_{\mathrm{Rx},\ell})\ \boldsymbol{c}_{\mathrm{Rx},\phi}(\boldsymbol{\Omega}_{\mathrm{Rx},\ell})] \in \mathcal{C}^{M_2 \times 2} \tag{3}$$

represent the responses of the Tx and the Rx antenna arrays at the DoD $\boldsymbol{\Omega}_{\mathrm{Tx},\ell}$ and the DoA $\boldsymbol{\Omega}_{\mathrm{Rx},\ell}$, respectively. Here, $\boldsymbol{c}_{\mathrm{Tx/Rx},\theta}(\cdot)$ and $\boldsymbol{c}_{\mathrm{Tx/Rx},\phi}(\cdot)$ are referred to as the array response at the vertical polarization θ and the horizontal polarization ϕ, respectively, for either the Tx or the Rx side. The parameters of the ℓth path $\boldsymbol{\psi}_\ell = [\tau_\ell, \upsilon_\ell, \boldsymbol{\Omega}_{\mathrm{Tx},\ell}, \boldsymbol{\Omega}_{\mathrm{Rx},\ell}, \boldsymbol{A}_\ell]$ include delay τ_ℓ, Doppler frequency υ_ℓ, DoD $\boldsymbol{\Omega}_{\mathrm{Tx},\ell}$, DoA $\boldsymbol{\Omega}_{\mathrm{Rx},\ell}$, and complex polarization matrix $\boldsymbol{A}_\ell$, which is written as[1]

$$\boldsymbol{A}_\ell = \begin{bmatrix} a_{\ell,\theta,\theta} & a_{\ell,\theta,\phi} \\ a_{\ell,\phi,\theta} & a_{\ell,\phi,\phi} \end{bmatrix} \in \mathcal{C}^{2\times 2} \tag{4}$$

where $\alpha_{\ell,p_{\mathrm{Rx}},p_{\mathrm{Tx}}}$ with $p_{\mathrm{Rx}}, p_{\mathrm{Tx}} \in \{\theta, \phi\}$ represents the complex attenuation coefficient experienced by the signal transmitted with specific Tx polarization p_{Tx} and Rx polarization p_{Rx} for the ℓth path. It is worth mentioning that $\boldsymbol{A}_\ell$ can be adapted for any two orthogonal polarizations, such as $p_{\mathrm{Rx}}, p_{\mathrm{Tx}} \in \{+45^\circ, -45^\circ\}$. The modeling approach proposed here is applicable to those cases as well. The diagonal entries of $\boldsymbol{A}_\ell$ are called co-polarized components and the nondiagonal entries are called cross-polarized components. A generic parametric model of $\boldsymbol{A}_\ell$ usually adopted in the geometry-based stochastic channel models (GSCMs) such as those described in [24], [25], [28], and [36] can be written as

$$\boldsymbol{A}_\ell = a_\ell \begin{bmatrix} \exp\{j\Phi_{\ell,\theta,\theta}\} & \sqrt{\frac{1}{\chi_\ell \eta_{\ell,\phi}}} \exp\{j\Phi_{\ell,\theta,\phi}\} \\ \sqrt{\frac{1}{\eta_{\ell,\theta}}} \exp\{j\Phi_{\ell,\phi,\theta}\} & \sqrt{\frac{1}{\chi_\ell}} \exp\{j\Phi_{\ell,\phi,\phi}\} \end{bmatrix} \tag{5}$$

where a_ℓ denotes the magnitude of $a_{\ell,\theta,\theta}$, $\Phi_{\ell,p_{\mathrm{Rx}},p_{\mathrm{Tx}}}$ with $p_{\mathrm{Rx}}, p_{\mathrm{Tx}} \in \{\theta, \phi\}$ is the initial phase of the channel with different Tx–Rx polarizations, $\eta_{\theta/\phi}$ represents the XPR for the

[1]The optics community calls $\boldsymbol{A}_\ell$ for the Jones matrix after Jones who originally proposed it in [35]. In [15], [24], and [29], the matrix is referred to as the polarization coupling matrix.

transmitted waves either θ-polarized or ϕ-polarized, and χ is the power ratio of the diagonal elements of $\boldsymbol{A}_\ell$, i.e., CPR. In the standard GSCMs, $\Phi_{\ell,p_{\mathrm{Rx}},p_{\mathrm{Tx}}}$ are independent and identically distributed (i.i.d.) random variables following uniform distribution within $[-\pi,\pi)$, and η_θ, η_ϕ are log-normal-distributed with statistical parameters specified for certain typical propagation scenarios.

B. Polarization Ellipse and Its Geometrical Parameters

Conventionally, the statistical behavior of $\boldsymbol{A}_\ell$ is described by the correlation of its entries and the power ratio of co-polarized components to cross-polarized components, i.e., the XPR. However, the effects of the polarization distortion in some other aspects, e.g., the power imbalance behavior among the polarization components and the left- or right-hand rotation characteristics of the elliptically polarized wave, are not appreciable by such characterization methods. It is necessary to find an alternative parametric approach that allows characterizing the polarization distortions in the channel more comprehensively than using the WINNER XPR models or the WINNER-extended XPR-CPR-based models.

It is obvious that the two entries in each column of $\boldsymbol{A}_\ell$ represent, respectively, the θ- and ϕ-polarized components received at the Rx when a linearly polarized wave with unit amplitude and zero initial phase is transmitted. These two complex-valued numbers can be used to retrieve the trajectory of the electric field intensity $\boldsymbol{E}$ on a plane perpendicular to the DoA $\boldsymbol{\Omega}_{\mathrm{Rx},\ell}$. Let us consider an example where a θ-polarized wave of unit amplitude and zero initial phase propagates along the ℓth path from the Tx to the Rx. The wave received at the Rx can be decomposed into θ- and ϕ-polarized components, with their complex attenuation coefficients represented by the entries in the first column of $\boldsymbol{A}_\ell$, i.e., $a_{\ell,\theta,\theta}$ and $a_{\ell,\phi,\theta}$, respectively. The corresponding complex-valued electric field intensity $\boldsymbol{E}_{\ell,\theta}$ observed at the location of the Rx antenna array on the plane perpendicular to $\boldsymbol{\Omega}_{\mathrm{Rx},\ell}$ can be written as

$$\boldsymbol{E}_{\ell,\theta} = (\boldsymbol{e}_\theta E_{\ell,\theta,\theta} + \boldsymbol{e}_\phi E_{\ell,\phi,\theta}) \exp\{-j\kappa z_\ell\} \tag{6}$$

where $\boldsymbol{e}_\theta$ and $\boldsymbol{e}_\phi$ denote the vertical and horizontal unit vectors, respectively, $E_{\ell,\theta,\theta}$ and $E_{\ell,\phi,\theta}$ represent the components of $\boldsymbol{E}_{\ell,\theta}$ along $\boldsymbol{e}_\theta$ and $\boldsymbol{e}_\phi$, respectively, κ is the wave number, and z_ℓ represents the length in meters of the ℓth path, which is equal to $\tau_\ell \cdot c$ with c denoting the speed of light. The variable t is dropped in (6) under the consideration that the received wave is time-harmonic and characterized with temporal behavior independent of $\boldsymbol{A}_\ell$[2]. Compared with the expression of $\boldsymbol{s}(t;\psi_\ell)$ in (1), it can be shown that

$$E_{\ell,\theta,\theta} = a_{\ell,\theta,\theta} \tag{7}$$

$$E_{\ell,\phi,\theta} = a_{\ell,\phi,\theta}. \tag{8}$$

[2]The time-dependent phase variation may also involve the phase drift caused by the nonzero Doppler frequency of the path. In such cases, the temporal phase variations can be calculated with z_ℓ being a function of the Doppler frequency of the path.

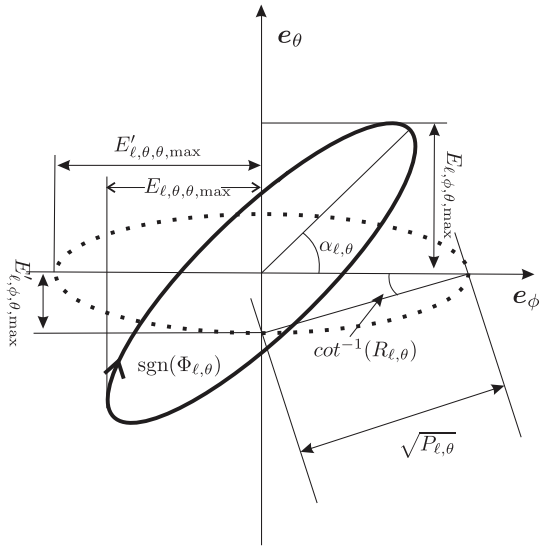

Fig. 1. Ellipse characterizing the polarization status of an EM wave.

The real-valued instantaneous representation $\boldsymbol{E}_{\ell,\theta}(t)$ of $\boldsymbol{E}_{\ell,\theta}$ is written as

$$\boldsymbol{E}_{\ell,\theta}(t) = \boldsymbol{e}_\theta E_{\ell,\theta,\theta}(t) + \boldsymbol{e}_\phi E_{\ell,\phi,\theta}(t) \tag{9}$$

with

$$\begin{aligned} E_{\ell,\phi,\theta}(t) &= \mathcal{R}\left\{\sqrt{2}E_{\ell,\phi,\theta}\exp\{j\omega t\}\right\} \\ &= E_{\ell,\phi,\theta,\max}\cos(\omega t - kz_\ell + \Phi^0_{\ell,\theta}) \end{aligned} \tag{10}$$

$$\begin{aligned} E_{\ell,\theta,\theta}(t) &= \mathcal{R}\left\{\sqrt{2}E_{\ell,\theta,\theta}\exp\{j\omega t\}\right\} \\ &= E_{\ell,\theta,\theta,\max}\cos(\omega t - kz_\ell + \Phi^0_{\ell,\theta} + \Phi_{\ell,\theta}) \end{aligned} \tag{11}$$

where $\mathcal{R}\{\cdot\}$ denotes the real part of the given complex number, $\omega = 2\pi f$ is the radian frequency with f being the carrier frequency, and $E_{\ell,\phi,\theta,\max}$ and $E_{\ell,\theta,\theta,\max}$ represent the maxima of magnitude calculated as

$$E_{\ell,\phi,\theta,\max} = \sqrt{2}|E_{\ell,\phi,\theta}| = \sqrt{2}|a_{\ell,\phi,\theta}| \tag{12}$$

$$E_{\ell,\theta,\theta,\max} = \sqrt{2}|E_{\ell,\theta,\theta}| = \sqrt{2}|a_{\ell,\theta,\theta}| \tag{13}$$

respectively. $\Phi^0_{\ell,\theta}$ in (10) and (11) denotes the phase of $a_{\ell,\theta,\theta}$, and the phase difference $\Phi_{\ell,\theta}$ between $E_{\ell,\theta,\theta}$ and $E_{\ell,\phi,\theta}$ is calculated as

$$\Phi_{\ell,\theta} = \arg\{\alpha_{\ell,\theta,\theta}\alpha^*_{\ell,\phi,\theta}\} \tag{14}$$

with $(\cdot)^*$ representing the complex conjugate and $\arg\{\cdot\}$ denoting the phase of given argument. From (10) and (11), it can be shown that $E_{\ell,\phi,\theta}(t)$ and $E_{\ell,\theta,\theta}(t)$ satisfy the following equation [37]:

$$\begin{aligned} &\frac{E^2_{\ell,\theta,\theta}(t)}{E^2_{\ell,\theta,\theta,\max}} + \frac{E^2_{\ell,\phi,\theta}(t)}{E^2_{\ell,\phi,\theta,\max}} \\ &\qquad - \frac{2E_{\ell,\theta,\theta}(t)E_{\ell,\phi,\theta}(t)}{E_{\ell,\theta,\theta,\max}E_{\ell,\phi,\theta,\max}}\cos\Phi_{\ell,\theta} = \sin^2\Phi_{\ell,\theta} \end{aligned} \tag{15}$$

which implies that the trajectory of the resultant electric field intensity $\boldsymbol{E}_{\ell,\theta}(t)$ follows an ellipse. Fig. 1 depicts an example of the trajectory of $\boldsymbol{E}_{\ell,\theta}(t)$ in solid curves calculated from (15).

Since the electric field intensity vectors for impinging waves oscillate along elliptical trajectories, it is natural to consider that each column of the polarization matrix $\boldsymbol{A}_\ell$ specifies how a linearly polarized wave is transformed to an elliptically polarized wave after propagation. An ellipse can be parameterized uniquely by a certain number of geometry-based parameters, which inspires the idea that the statistics of these parameters extracted from measurements may be used as a stochastic model for per-path polarizations. In the following, we briefly review the ellipse parameters of interest for modeling, and derive the relationship between these parameters and the entries in $\boldsymbol{A}_\ell$.

An ellipse characterizing the polarization of the wave propagating along the ℓth path is determined by four parameters: 1) the ratio $R_\ell \in [1, \infty)$ of the length for its semimajor to semiminor axes, which is applied as a measure of the ellipse ovality; 2) the size of the ellipse defined to be the sum of the squared length of the semimajor and semiminor axes, which can also be called as the power P_ℓ of the wave in our case; 3) the tilt angle α_ℓ referred to as the angle from the ϕ-polarization axis to the major axis; and 4) finally, the sign $\text{sgn}(\Phi_\ell) \in \{-1, 1\}$ of phase difference Φ_ℓ between the components received at two orthogonal polarizations. It is obvious that R_ℓ, P_ℓ, and α_ℓ determine jointly the shape and the attitude of the ellipse in a plane, and $\text{sgn}(\Phi_\ell)$ indicates whether the elliptical-polarized wave is left- or right-hand-rotated. Notice that a circle and a line can also be considered as special ellipses with $R_\ell = 1$ and ∞, respectively. For notational convenience, we use $\boldsymbol{\vartheta}_{\ell,\theta} = (P_{\ell,\theta}, \alpha_{\ell,\theta}, R_{\ell,\theta}, \text{sgn}(\Phi_{\ell,\theta}))$ to denote the parameter vector characterizing the polarization ellipse for the received wave when it is originally transmitted with θ-polarization, and $\boldsymbol{\vartheta}_{\ell,\phi} = (P_{\ell,\phi}, \alpha_{\ell,\phi}, R_{\ell,\phi}, \text{sgn}(\Phi_{\ell,\phi}))$ for the wave being transmitted with ϕ-polarization. The analytical expressions of $\boldsymbol{\vartheta}_{\ell,\theta}$ and $\boldsymbol{\vartheta}_{\ell,\phi}$ as functions of $\boldsymbol{A}_\ell$ are necessary, since channel parameter estimation algorithms usually provide the estimate of $\boldsymbol{A}_\ell$ first. However, such expressions have not been found in literature. Thus, we derive the expressions and shortly present the procedure below.

Let us still consider the example where the entries in the first column of $\boldsymbol{A}_\ell$, i.e., $a_{\ell,\theta,\theta}$ and $a_{\ell,\phi,\theta}$ are known, and the expressions of $\boldsymbol{\vartheta}_{\ell,\theta}$ as functions of $\boldsymbol{A}_\ell$ are expected. According to the aforementioned analysis, the phase difference $\Phi_{\ell,\theta}$ can be calculated from (14). Thus, $\text{sgn}(\Phi_\theta)$ can be easily obtained. For expressions of the other entries of $\boldsymbol{\vartheta}_{\ell,\theta}$, it is necessary to introduce a "standard" ellipse which is illustrated in dotted curve in Fig. 1. This standard ellipse with the same shape as the ellipse in solid curve has the semimajor axis coincident with the ϕ-polarization axis. It is obvious that the ellipse in solid curve in Fig. 1 can be obtained by rotating the standard ellipse counterclockwise by the angle equal to the tilt angle $\alpha_{\ell,\theta}$. We use

$$\boldsymbol{E}'_{\ell,\theta}(t) = \boldsymbol{e}_\theta E'_{\ell,\theta,\theta}(t) + \boldsymbol{e}_\phi E'_{\ell,\phi,\theta}(t) \tag{16}$$

to denote the real-valued instantaneous electric field intensity vector which oscillates along the standard ellipse. The corresponding complex-valued representation can be written as

$$\boldsymbol{E}'_{\ell,\theta} = \left(\boldsymbol{e}_\theta E'_{\ell,\theta,\theta} + \boldsymbol{e}_\phi E'_{\ell,\phi,\theta}\right) \exp\{-j\kappa z_\ell\}. \tag{17}$$

Similar with the aforementioned analysis, $E'_{\ell,\theta,\theta}(t)$ and $E'_{\ell,\phi,\theta}(t)$ satisfy the following equation:

$$\frac{(E'_{\ell,\theta,\theta}(t))^2}{\left(E'_{\ell,\theta,\theta,\max}\right)^2} + \frac{(E'_{\ell,\phi,\theta}(t))^2}{\left(E'_{\ell,\phi,\theta,\max}\right)^2} = 1 \tag{18}$$

where $E'_{\ell,\theta,\theta,\max}$ and $E'_{\ell,\phi,\theta,\max}$ represent the maximal lengths of the trajectory along $\boldsymbol{e}_\theta$ and $\boldsymbol{e}_\phi$ axes, respectively. Here, we assume that the semiminor axis of the standard ellipse coincides with $\boldsymbol{e}_\theta$, and thus, the inequality $E'_{\ell,\theta,\theta,\max} \le E'_{\ell,\phi,\theta,\max}$ holds. As shown in Appendix A, $E'_{\ell,\phi,\theta,\max}$ and $E'_{\ell,\theta,\theta,\max}$ can be calculated as, respectively,

$$E'_{\ell,\phi,\theta,\max} = \max\left[r_\ell\left(\tan(\varphi_{\ell,1,\theta})\right), r_\ell\left(\tan(\varphi_{\ell,2,\theta})\right)\right] \tag{19}$$

$$E'_{\ell,\theta,\theta,\max} = \min\left[r_\ell(\tan(\varphi_{\ell,1,\theta})), r_\ell(\tan(\varphi_{\ell,2,\theta}))\right] \tag{20}$$

with $\max[\cdot]$ and $\min[\cdot]$ representing the maximum and minimum of given arguments, respectively, and

$$r_\ell(x) = \sqrt{\frac{(1+x^2)}{(\xi_{\ell,1,\theta}x^2 - \xi_{\ell,2,\theta}x + \xi_{\ell,3,\theta})}}. \tag{21}$$

Here, $\varphi_{\ell,1,\theta}$, $\varphi_{\ell,2,\theta}$ in (19) and (20) and $\xi_{\ell,1,\theta}$, $\xi_{\ell,2,\theta}$, $\xi_{\ell,3,\theta}$ in (21) are calculated as

$$\varphi_{\ell,1,\theta} = \frac{1}{2}\tan^{-1}\left(\frac{2E_{\ell,\theta,\theta,\max}E_{\ell,\phi,\theta,\max}\cos\Phi_{\ell,\theta}}{E^2_{\ell,\phi,\theta,\max} - E^2_{\ell,\theta,\theta,\max}}\right) \tag{22}$$

$$\varphi_{\ell,2,\theta} = \varphi_{\ell,1,\theta} + \frac{\pi}{2} \tag{23}$$

$$\xi_{\ell,1,\theta} = \frac{1}{E^2_{\ell,\theta,\theta,\max}\sin^2\Phi_{\ell,\theta}} \tag{24}$$

$$\xi_{\ell,2,\theta} = \frac{2\cos\Phi_{\ell,\theta}}{E_{\ell,\theta,\theta,\max}E_{\ell,\phi,\theta,\max}\sin^2\Phi_{\ell,\theta}} \tag{25}$$

$$\xi_{\ell,3,\theta} = \frac{1}{E^2_{\ell,\phi,\theta,\max}\sin^2\Phi_{\ell,\theta}} \tag{26}$$

provided the first column of $\boldsymbol{A}_\ell$ is available. It is proved in Appendix A that the tilt angle equals one of $\varphi_{\ell,1,\theta}$ and $\varphi_{\ell,2,\theta}$, which yields the equality $r_\ell(\tan(\varphi_{\ell,i,\theta})) = E'_{\ell,\phi,\theta,\max}$, $i \in \{1, 2\}$, i.e.,

$$\alpha_{\ell,\theta} = \left\{\varphi_{\ell,i,\theta} : r_\ell\left(\tan(\varphi_{\ell,i,\theta})\right) = E'_{\ell,\phi,\theta,\max}, i = 1, 2\right\}.$$

The ovality $R_{\ell,\theta}$ and the size $P_{\ell,\theta}$ of the ellipse can be calculated from (19) and (20), respectively, as

$$R_{\ell,\theta} = \frac{E'_{\ell,\phi,\theta,\max}}{E'_{\ell,\theta,\theta,\max}} \tag{27}$$

$$P_{\ell,\theta} = \frac{1}{2}\left[(E'_{\ell,\theta,\theta,\max})^2 + (E'_{\ell,\phi,\theta,\max})^2\right]. \tag{28}$$

Here, the so-called ellipse size $P_{\ell,\theta}$ is equivalent with the average power of the received signal when the unit power signal is transmitted with a specific p_{Tx}-polarization.

Similarly, the parameters $\boldsymbol{\vartheta}_{\ell,\phi}$ can be calculated from $a_{\ell,\theta,\phi}$ and $a_{\ell,\phi,\phi}$ by using (19)–(28) with necessary adaptation.

C. Retrieving Polarization Matrix $\boldsymbol{A}_\ell$ From Elliptical Parameters $\boldsymbol{\vartheta}_{\ell,\theta}$ and $\boldsymbol{\vartheta}_{\ell,\phi}$

When implementing the stochastic polarization models with statistics of $\boldsymbol{\vartheta}_{\ell,\theta}$ and $\boldsymbol{\vartheta}_{\ell,\phi}$ for channel simulations, $\boldsymbol{A}_\ell$ needs to be calculated from the random realizations of $\boldsymbol{\vartheta}_{\ell,\theta}$ and $\boldsymbol{\vartheta}_{\ell,\phi}$ that are generated based on the model. In the following, we derive $a_{\ell,\theta,\theta}$ and $a_{\ell,\phi,\theta}$ based on $\boldsymbol{\vartheta}_{\ell,\theta}$ specified for the ℓ path. The expression of $a_{\ell,\theta,\phi}$ and $a_{\ell,\phi,\phi}$ as functions of $\boldsymbol{\vartheta}_{\ell,\phi}$ can be found similarly. First, by solving the system of equations

$$\begin{cases} R_{\ell,\theta} = \dfrac{E'_{\ell,\phi,\theta,\max}}{E'_{\ell,\theta,\theta,\max}} \\ P_{\ell,\theta} = \dfrac{1}{2}\left[(E'_{\ell,\theta,\theta,\max})^2 + (E'_{\ell,\phi,\theta,\max})^2\right] \end{cases} \tag{29}$$

we obtain

$$E'_{\ell,\phi,\theta,\max} = R_{\ell,\theta}\sqrt{\frac{2P_{\ell,\theta}}{\left(1+R_{\ell,\theta}^2\right)}} \tag{30}$$

$$E'_{\ell,\theta,\theta,\max} = \sqrt{\frac{2P_{\ell,\theta}}{\left(1+R_{\ell,\theta}^2\right)}}. \tag{31}$$

From (18), it can be shown that

$$\begin{aligned} E'_{\ell,\phi,\theta} &= 2^{-1/2}E'_{\ell,\phi,\theta,\max}\exp\left\{j\Phi^0_{\ell,\theta}\right\} \\ &= R_{\ell,\theta}\sqrt{\frac{P_{\ell,\theta}}{(1+R_{\ell,\theta}^2)}}\exp\left\{j\Phi^0_{\ell,\theta}\right\} \end{aligned} \tag{32}$$

$$\begin{aligned} E'_{\ell,\theta,\theta} &= 2^{-1/2}E'_{\ell,\theta,\theta,\max}\exp\left\{j\left[\Phi^0_{\ell,\theta} + \operatorname{sgn}(\Phi_{\ell,\theta})\frac{\pi}{2}\right]\right\} \\ &= \sqrt{\frac{P_{\ell,\theta}}{(1+R_{\ell,\theta}^2)}}\exp\left\{j\left[\Phi^0_{\ell,\theta} + \operatorname{sgn}(\Phi_{\ell,\theta})\frac{\pi}{2}\right]\right\} \end{aligned} \tag{33}$$

where $\Phi^0_{\ell,\theta}$ can be generated as a random variable uniformly distributed within $[0, 2\pi)$. The complex-valued vector $[E_{\ell,\phi,\theta}, E_{\ell,\theta,\theta}]^{\mathrm{T}}$ with $(\cdot)^{\mathrm{T}}$ denoting the transpose operation is calculated via rotating $[E'_{\ell,\phi,\theta}, E'_{\ell,\theta,\theta}]^{\mathrm{T}}$ counter-clockwise by the tilt angle $\alpha_{\ell,\theta}$, i.e.,

$$\begin{bmatrix} E_{\ell,\phi,\theta} \\ E_{\ell,\theta,\theta} \end{bmatrix} = \begin{bmatrix} \cos(\alpha_{\ell,\theta}) & -\sin(\alpha_{\ell,\theta}) \\ \sin(\alpha_{\ell,\theta}) & \cos(\alpha_{\ell,\theta}) \end{bmatrix} \begin{bmatrix} E'_{\ell,\phi,\theta} \\ E'_{\ell,\theta,\theta} \end{bmatrix} \tag{34}$$

which yields for $E_{\ell,\phi,\theta}$ and $E_{\ell,\theta,\theta}$

$$E_{\ell,\phi,\theta} = {P_{\ell,\theta}}^{1/2}\left(1+R_{\ell,\theta}^2\right)^{-1/2}[-1 \quad R_{\ell,\theta}]\boldsymbol{\xi}_{\ell,\theta} \tag{35}$$

$$E_{\ell,\theta,\theta} = {P_{\ell,\theta}}^{1/2}\left(1+R_{\ell,\theta}^2\right)^{-1/2}[R_{\ell,\theta} \quad 1]\boldsymbol{\xi}_{\ell,\theta} \tag{36}$$

with

$$\boldsymbol{\xi}_{\ell,\theta} = \begin{bmatrix} \sin(\alpha_{\ell,\theta})\exp\left\{j\left(\Phi^0_{\ell,\theta} + \operatorname{sgn}(\Phi_{\ell,\theta})\frac{\pi}{2}\right)\right\} \\ \cos(\alpha_{\ell,\theta})\exp\left\{j\Phi^0_{\ell,\theta}\right\} \end{bmatrix}. \tag{37}$$

Similarly, it can be shown that

$$E_{\ell,\theta,\phi} = {P_{\ell,\phi}}^{1/2}\left(1+R_{\ell,\phi}^2\right)^{-1/2}[R_{\ell,\phi} \;\; 1]\,\boldsymbol{\xi}_{\ell,\phi}, \tag{38}$$

$$E_{\ell,\phi,\phi} = {P_{\ell,\phi}}^{1/2}\left(1+R_{\ell,\phi}^2\right)^{-1/2}[-1 \quad R_{\ell,\phi}]\,\boldsymbol{\xi}_{\ell,\phi} \tag{39}$$

with

$$\boldsymbol{\xi}_{\ell,\phi} = \begin{bmatrix} \sin(\alpha_{\ell,\phi})\exp\left\{j\left(\Phi^0_{\ell,\phi} + \operatorname{sgn}(\Phi_{\ell,\phi})\frac{\pi}{2}\right)\right\} \\ \cos(\alpha_{\ell,\phi})\exp\left\{j\Phi^0_{\ell,\phi}\right\} \end{bmatrix} \tag{40}$$

and $\Phi^0_{\ell,\phi}$ is an initial phase for waves transmitted with ϕ-polarization, which can be generated as a random variable uniformly distributed within $[0, 2\pi)$. By equating $\alpha_{\ell,p_{\mathrm{Rx}},p_{\mathrm{Tx}}}$ with $E_{\ell,p_{\mathrm{Rx}},p_{\mathrm{Tx}}}$, $p_{\mathrm{Rx}}, p_{\mathrm{Tx}} \in \{\theta, \phi\}$ calculated based on (35)–(40); the entries of $\boldsymbol{A}_\ell$ are finally obtained.

D. Retrieving the XPR and CPR Parameters From Elliptical Parameters $\boldsymbol{\vartheta}_{\ell,\theta}$ and $\boldsymbol{\vartheta}_{\ell,\phi}$

The conventional GSCMs, such as WINNER SCMEs, characterize per-path polarization for XPRs and CPR, which are calculated as [15], [16]

$$\eta_{\ell,\theta} = \frac{|\alpha_{\ell,\theta,\theta}|^2}{|\alpha_{\ell,\phi,\theta}|^2}, \eta_{\ell,\phi} = \frac{|\alpha_{\ell,\phi,\phi}|^2}{|\alpha_{\ell,\theta,\phi}|^2}, \chi_\ell = \frac{|\alpha_{\ell,\theta,\theta}|^2}{|\alpha_{\ell,\phi,\phi}|^2} \tag{41}$$

where $\eta_{\ell,\theta}$, $\eta_{\ell,\phi}$ represent the XPR for waves transmitted with θ- and ϕ-polarization, respectively, and χ_ℓ is the CPR describes the power imbalance in two copolarized components. Given $\boldsymbol{\vartheta}_{\ell,\theta}$ and $\boldsymbol{\vartheta}_{\ell,\phi}$, the XPRs and CPR can be calculated from (41) with $\alpha_{\ell,p_{\mathrm{Tx}},p_{\mathrm{Rx}}}$ substituted by

$$\alpha_{\ell,\theta,\theta} = {P_{\ell,\theta}}^{1/2}\left(1+R_{\ell,\theta}^2\right)^{-1/2}[R_{\ell,\theta} \quad 1]\boldsymbol{\xi}_{\ell,\theta} \tag{42}$$

$$\alpha_{\ell,\phi,\theta} = {P_{\ell,\theta}}^{1/2}\left(1+R_{\ell,\theta}^2\right)^{-1/2}[-1 \quad R_{\ell,\theta}]\boldsymbol{\xi}_{\ell,\theta} \tag{43}$$

$$\alpha_{\ell,\theta,\phi} = {P_{\ell,\phi}}^{1/2}\left(1+R_{\ell,\phi}^2\right)^{-1/2}[R_{\ell,\phi} \;\; 1]\boldsymbol{\xi}_{\ell,\phi} \tag{44}$$

$$\alpha_{\ell,\phi,\phi} = {P_{\ell,\phi}}^{1/2}\left(1+R_{\ell,\phi}^2\right)^{-1/2}[-1 \quad R_{\ell,\phi}]\boldsymbol{\xi}_{\ell,\phi} \tag{45}$$

where $\boldsymbol{\xi}_{\ell,\theta}$ and $\boldsymbol{\xi}_{\ell,\phi}$ are calculated by using (37) and (40), respectively.

It is worth mentioning that deriving the analytical expressions of $\boldsymbol{\vartheta}_{\ell,\theta}$ and $\boldsymbol{\vartheta}_{\ell,\phi}$ in terms of XPRs and CPR is impossible, as XPRs and CPR do not contain the complete information of a polarization matrix required for computing elliptical parameters. However, it is possible to calculate $\boldsymbol{\vartheta}_{\ell,\theta}$ and $\boldsymbol{\vartheta}_{\ell,\phi}$ from $\boldsymbol{A}_\ell$ generated by using (4) with specific $\eta_{\ell,\theta}$, $\eta_{\ell,\phi}$, χ_ℓ given the values of initial phases $\Phi_{\ell,p_{\mathrm{Tx}},p_{\mathrm{Rx}}}$, $p_{\mathrm{Rx}}, p_{\mathrm{Tx}} \in \{\theta, \phi\}$.

E. Proposed Stochastic Elliptical-Parameter-Based Polarization Model and Its Implementation in Channel Simulation

The statistical polarization model proposed here is established in the two steps. 1) Channel measurement data obtained in environments of specific type is processed by using high-resolution parameter estimation algorithms, such as the SAGE algorithm [33]. Then, from the estimated polarization matrix of individual paths, the ellipse parameters $\boldsymbol{\vartheta}_{\ell,\theta}$ and $\boldsymbol{\vartheta}_{\ell,\phi}$ are calculated for MPCs. 2) Based on a sufficient number of estimated MPCs, the statistics of $\boldsymbol{\vartheta}_{\ell,\theta}$ and $\boldsymbol{\vartheta}_{\ell,\phi}$ are extracted, including empirical probability density functions (pdfs) of parameters in

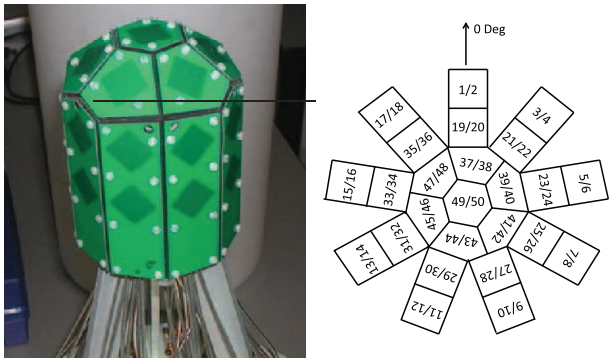

(a) (b)

Fig. 2. (a) Photograph and (b) antenna indices of the 50-element antenna array used in the Tx and Rx of the channel sounder.

$\boldsymbol{\vartheta}_{\ell,\theta}$ and $\boldsymbol{\vartheta}_{\ell,\phi}$. Analytical pdfs may be applied to fit with the empirical pdfs to maintain the simplicity of resultant models.

The established stochastic polarization models can be used in channel simulations as a supplementary to the existing standard GSCMs. The parameters except the polarization matrix can still be generated by using the GSCMs. The polarization matrices of individual paths are created separately by using the stochastic polarization models in the following two steps. 1) The ellipse parameters $\boldsymbol{\vartheta}_{\ell,\theta}$ and $\boldsymbol{\vartheta}_{\ell,\phi}$ for MPCs are first randomly generated based on the statistics specified in the model. 2) Then, the entries in the first and second columns of each polarization matrix are calculated from the corresponding ellipse parameters $\boldsymbol{\vartheta}_{\ell,\theta}$ and $\boldsymbol{\vartheta}_{\ell,\phi}$, respectively, by using the results presented in Section II-C.

III. Empirical Stochastic Polarization Models for Indoor Scenarios

In this section, the modeling approach proposed here is applied to establish some empirical stochastic propagation models based on wideband channel measurements. Different statistics of the ellipse parameters observed from indoor scenarios of various types demonstrate the necessity of refined modeling of the polarizations using the proposed approach.

A. Measurement Equipment and Environments

The measurements were performed by Elektrobit Oy and Technology University of Vienna in 2005 using the wideband MIMO channel sounder—PROPSound—in a building at Oulu University. A 50-element and a 32-element patch-antenna arrays were used in the Tx and Rx, respectively. The photograph illustrated in Fig. 2(a) depicts the appearance of the 50-element array. Fig. 2(b) shows the indices of antennas on the array. The 32-element Rx array has the same configuration as the 50-element Tx array. However, the antennas from No. 19–36 were not activated for receiving signals during the measurement. Each patch in the array consists of two antennas which are $+45^\circ$ and -45° polarized, respectively. The measurements were conducted with effective bandwidth of 100 MHz at the carrier frequency of 5.25 GHz. The sounding of individual subchannels between any pair of Tx and Rx antennas is performed sequentially in a time-division-multiplexing (TDM) mode. During the measurements, the Tx and Rx were loaded in two trolleys, respectively. The Tx trolley moved in a constant speed along predefined routes, whereas the Rx trolley was kept stationary. The initialization-and-search-improved SAGE (ISI-SAGE) algorithm was used to estimate individual path parameters from raw measurement data [33]. Table I reports the relevant settings for the measurements and in the procedure of parameter estimation. The readers interested at the detailed information of the measurement campaign are referred to [38, Sec. III].

TABLE I
Measurement and Parameter Estimation Settings

Measurement settings	Values/configurations
Carrier frequency	5.25 GHz
Effective bandwidth	100 MHz
Chip rate	100 Mchip/s
Code length	255 chips
Sampling frequency in the Rx	200 MHz
Transmission power	26 dBm
Polarizations of antennas	$\pm 45^\circ$
Tx antenna switch sequence	$1, 2, ..., 50$
Rx antenna switch sequence	$1, 2, ...18, 37, ...50$
Measurement cycle duration*	8.42 ms
Tx height	1.53 m
Rx height	1.05 m
Trolley moving speed	0.5 m/s
Parameter estimation settings	**Values/configurations**
No. of paths to estimate	50
Azimuth estimation range	$[-180^\circ, 180^\circ]$
Elevation estimation range	$[-70^\circ, 90^\circ]$
Estimated polarizations	Vertical and horizontal

*"Measurement cycle duration" refers to the duration within which the channels between any possible pairs of the Tx and Rx antennas are measured once.

To investigate the statistics of $\boldsymbol{\vartheta}_{\ell,\theta}$ and $\boldsymbol{\vartheta}_{\ell,\phi}$ in various indoor environments, measurements in five indoor scenarios of different types are considered. Fig. 3 illustrates the premises of these scenarios. The Rx's location and the route along which the Tx trolley moved in each scenario are also depicted in Fig. 3. The scenarios (a)–(e) are, respectively, a long and narrow corridor, two corridors crossing each other, a laboratory with 1.5 m high metal furniture, a computer room, and a hall. In the scenario (a), the Tx and Rx were located in the same corridor, and they were separated by multiple doors with toughened glasses, leading to the obstructed line-of-sight (OLoS) between the Tx and the Rx. In the scenario (b), the Tx and Rx were located in two corridors perpendicularly connected, and in the most of time, no LoS exists between the Tx and Rx. To distinguish these two scenarios, we call them as OLoS corridor and non-LoS (NLoS) corridor, respectively. During the measurements, students kept doing experiments in the laboratory in the scenario (c) and people were wandering in the hall in the scenario (e). The movements of people and the mobility of the Tx trolley jointly created the randomness for the measured channels from one snapshot to another. About 1000 measurement snapshots were collected in each scenario.

B. Stochastic Polarization Models Extracted

The models are extracted in the following steps. First, the polarization matrices of paths in the channel are estimated by using the ISI-SAGE algorithm. The ellipse parameters

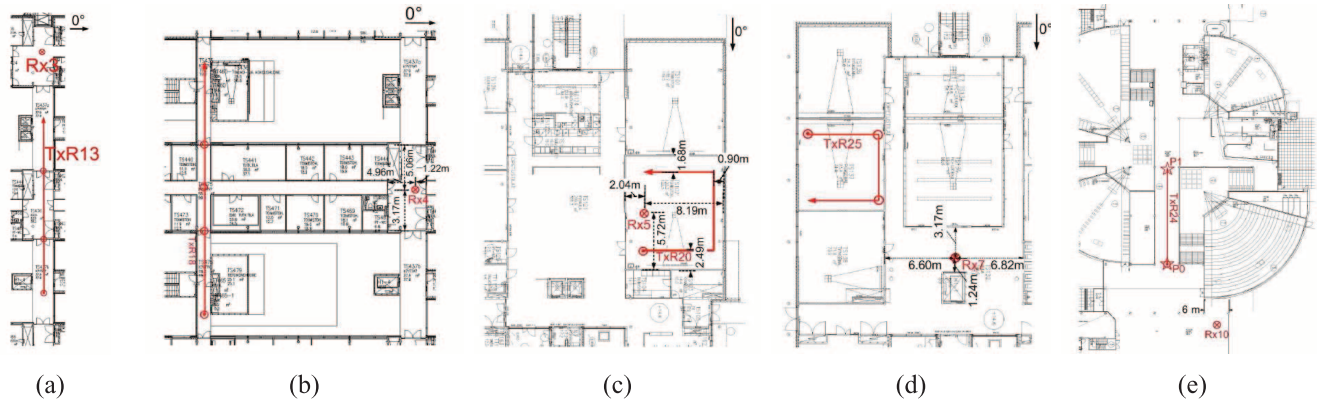

Fig. 3. Premises of the five indoor propagation scenarios considered for modeling. (a) OLoS corridor. (b) NLoS corridor. (c) Laboratory. (d) Computer room. (e) Hall.

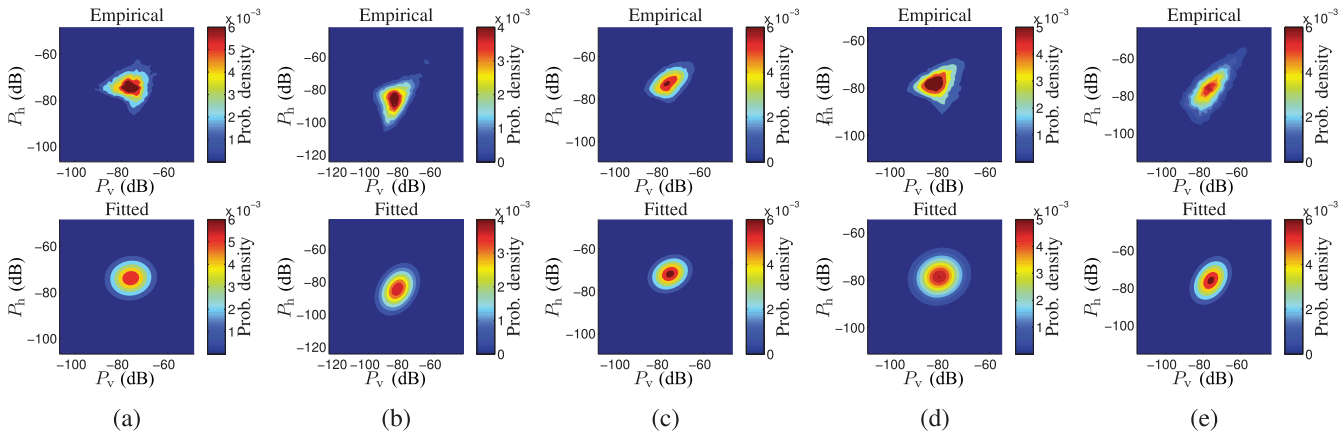

Fig. 4. Empirical joint pdf of $P_{\ell,\theta}$ and $P_{\ell,\phi}$ and fitted pdf for individual scenarios. (a) OLoS corridor. (b) NLoS corridor. (c) Students laboratory. (d) Computer room. (e) Cafeteria hall.

calculated from polarization matrices of estimated MPCs in all snapshots for one scenario are considered as the set of observations of $\boldsymbol{\vartheta}_{\ell,\theta}$ and $\boldsymbol{\vartheta}_{\ell,\phi}$. Based on these samples, the pdfs of the parameters in $\boldsymbol{\vartheta}_{\ell,\theta}$ and $\boldsymbol{\vartheta}_{\ell,\phi}$ are calculated. In order to find the simple analytical expressions for the pdfs, some standard pdfs with analytical expressions are selected to fit to the empirical data. These standard pdfs include the Gaussian, log-normal, Laplacian, Nakagami, and Rayleigh pdfs. Usually, for random variables with nonnegative values, such as power, magnitude, and ratio, the log-normal, Rayleigh, Rician, and m-Nakagami pdfs are used for fitting. For parameters with cyclic supports such as angular variables, Laplacian pdf or von-Mises pdf are adopted [16]. When the types of distribution functions selected for fitting the empirical distributions are specified, the parameters of pdfs were obtained using least squares estimation, e.g., by using the MATLAB function "nlinfit." Once the pdf parameters are determined, the Akaike information criterion (AIC) [39] is applied to choose the best fitted pdf among the candidates by considering the appropriate compromise between the likelihood of the fitted model and its complexity. In order to evaluate whether the selected pdf is consistent with the empirical pdf, the Kolmogorov–Smirnov testing is further used to judge whether the null hypothesis that both pdfs are drawn from the same distributions is true. Without specifically mentioning, the analytical pdfs presented in the following results have passed the Kolmogorov–Smirnov testing and proved to fit well with their empirical counterparts.

1) Statistics of $P_{\ell,\theta}$ and $P_{\ell,\phi}$: As shown in the model (1) of the received signal contributed by an MPC, the transmitted waves with θ- and ϕ-polarization propagate along the same route for a fixed path. Thus, it is natural to consider that $P_{\ell,\theta}$ and $P_{\ell,\phi}$ are correlated for the same path. Fig. 4(a)–(e) depicts, respectively, the empirical joint pdf $f(P_{\ell,\theta}, P_{\ell,\phi})$ of $P_{\ell,\theta}$ and $P_{\ell,\phi}$ for the five scenarios. The bivariate log-normal pdfs fitted to the empirical pdfs are also illustrated. We choose the log-normal distribution for fitting because the power of the four entries in $\boldsymbol{A}_\ell$ have been found to follow log-normal distributions. This leads to the conjecture that $P_{\ell,\theta}$ and $P_{\ell,\phi}$ are also log-normal-distributed [40], [41]. Table II reports the parameters of the log-normal pdfs fitted to the empirical pdfs. It is worth mentioning that the value of total path power, i.e., $P_{\ell,\theta} + P_{\ell,\phi}$ can be determined according to the existing SCMEs by using intercluster statistics. However, no explicit instructions are given in the standard SCMEs for further splitting the path power among the different polarized components. The pdfs $f(P_{\ell,\theta}, P_{\ell,\phi})$ presented here may be helpful when allocating the appropriate values of $P_{\ell,\theta}$ and $P_{\ell,\phi}$ for the MPCs propagating along the same path. It can be observed from Fig. 4

TABLE II
PARAMETERS OF DISTRIBUTIONS WITH ANALYTICAL PDF EXPRESSIONS FITTED TO THE EMPIRICAL PDFS, AND THE CROSS-CORRELATION COEFFICIENTS OF ELLIPTICAL PARAMETERS

Scenarios index and descriptions	(a) OLoS corridor	(b) NLoS corridor	(c) Student laboratory	(d) Computer room	(e) Cafeteria hall
Parameters of 2-D Gaussian distributions fitted to the empirical pdfs of $P_{\ell,\theta}$ and $P_{\ell,\phi}$					
ρ	0.1	0.6	0.4	0.2	0.7
μ_θ (dB)	–76.0	–82.4	–75.9	–80.9	–76.0
μ_ϕ (dB)	–73.9	–84.7	–71.9	–78.6	–76.1
σ_θ (dB)	6.0	8.4	6.0	6.3	7.6
σ_ϕ (dB)	5.1	9.7	5.2	5.8	8.8
Parameters of truncated Laplacian pdfs fitted to the empirical pdfs of tilt angle $\alpha_{\ell,\theta}$					
μ_{α_θ} (°)	94.1	90.7	90.2	95.1	91.2
b_{α_θ}	26.9	24.7	37.3	37.6	32.3
Parameters of truncated Laplacian pdfs fitted to the empirical pdfs of tilt angle $\alpha_{\ell,\phi}$					
μ_{α_ϕ} (°)	–4.5	–0.9	–1.0	–6.6	2.4
b_{α_ϕ}	23.3	25.8	27.4	28.3	24.2
Parameters of Rayleigh pdfs fitted to the empirical pdfs of the ovality parameters $R_{\ell,\theta}$ and $R_{\ell,\phi}$					
ϱ_{R_θ} for $R_{\ell,\theta}$	6.0	6.0	5.4	5.4	5.6
ϱ_{R_ϕ} for $R_{\ell,\phi}$	6.3	5.9	6.0	5.9	6.0
Cross-correlation coefficients of the parameters in $\boldsymbol{\vartheta}_{\ell,\theta}$					
$\rho_{P_{\ell,\theta},\alpha_{\ell,\theta}}$	–0.05	0.01	0.00	–0.05	0.04
$\rho_{P_{\ell,\theta},R_{\ell,\theta}}$	0.06	0.06	0.08	0.05	0.03
$\rho_{P_{\ell,\theta},\Phi_{\ell,\theta}}$	0.04	0.04	0.02	–0.03	0.03
$\rho_{\alpha_{\ell,\theta},R_{\ell,\theta}}$	–0.01	–0.02	0.01	–0.04	–0.02
$\rho_{\alpha_{\ell,\theta},\Phi_{\ell,\theta}}$	–0.04	–0.02	–0.01	0.03	–0.04
$\rho_{R_{\ell,\theta},\Phi_{\ell,\theta}}$	–0.01	–0.02	0.00	0.02	0.00
Cross-correlation coefficients of the parameters in $\boldsymbol{\vartheta}_{\ell,\phi}$					
$\rho_{P_{\ell,\phi},\alpha_{\ell,\phi}}$	0.02	0.01	0.00	0.03	0.01
$\rho_{P_{\ell,\phi},R_{\ell,\phi}}$	0.11	0.11	0.08	0.06	0.07
$\rho_{P_{\ell,\phi},\Phi_{\ell,\phi}}$	0.00	–0.08	–0.02	0.04	–0.05
$\rho_{\alpha_{\ell,\phi},R_{\ell,\phi}}$	0.01	–0.01	–0.01	0.03	–0.02
$\rho_{\alpha_{\ell,\phi},\Phi_{\ell,\phi}}$	–0.07	0.02	0.00	–0.10	0.00
$\rho_{R_{\ell,\phi},\Phi_{\ell,\phi}}$	–0.04	0.01	0.02	–0.08	0.03
Cross-correlation coefficients of the parameters in $\boldsymbol{\vartheta}_{\ell,\theta}$ and $\boldsymbol{\vartheta}_{\ell,\phi}$					
$\rho_{P_{\ell,\theta},P_{\ell,\phi}}$	0.11	0.63	0.44	0.19	0.69
$\rho_{P_{\ell,\theta},\alpha_{\ell,\phi}}$	–0.01	0.02	0.01	0.02	0.03
$\rho_{P_{\ell,\theta},R_{\ell,\phi}}$	–0.05	–0.03	–0.01	–0.07	–0.02
$\rho_{P_{\ell,\theta},\Phi_{\ell,\phi}}$	–0.05	–0.03	0.00	0.00	0.00
$\rho_{\alpha_{\ell,\theta},P_{\ell,\phi}}$	–0.03	0.02	–0.01	0.01	0.04
$\rho_{\alpha_{\ell,\theta},\alpha_{\ell,\phi}}$	0.13	0.06	0.02	0.14	0.04
$\rho_{\alpha_{\ell,\theta},R_{\ell,\phi}}$	–0.01	0.00	–0.01	0.01	–0.03
$\rho_{\alpha_{\ell,\theta},\Phi_{\ell,\phi}}$	0.03	0.00	–0.01	–0.05	0.00
$\rho_{R_{\ell,\theta},P_{\ell,\phi}}$	–0.07	–0.04	0.02	–0.04	–0.04
$\rho_{R_{\ell,\theta},\alpha_{\ell,\phi}}$	0.00	0.01	–0.01	–0.02	0.00
$\rho_{R_{\ell,\theta},R_{\ell,\phi}}$	0.00	0.01	0.02	0.01	0.03
$\rho_{R_{\ell,\theta},\Phi_{\ell,\phi}}$	–0.01	–0.01	0.00	0.02	–0.01
$\rho_{\Phi_{\ell,\theta},P_{\ell,\phi}}$	–0.04	0.01	0.02	0.01	–0.06
$\rho_{\Phi_{\ell,\theta},\alpha_{\ell,\phi}}$	–0.02	–0.02	0.00	–0.02	–0.04
$\rho_{\Phi_{\ell,\theta},R_{\ell,\phi}}$	0.01	0.00	0.02	–0.01	0.04
$\rho_{\Phi_{\ell,\theta},\Phi_{\ell,\phi}}$	–0.01	0.01	0.03	0.05	0.04

$\boxed{\cdots}$: The highest absolute cross-correlation value in a scenario.

that except for the corridor scenarios, $f(P_{\ell,\theta}, P_{\ell,\phi})$ are more or less tilted, implying that $P_{\ell,\theta}$ and $P_{\ell,\phi}$ are less-correlated in a closed environment, e.g., with waveguide structures as in the OLoS corridor. Our explanation for this phenomenon is that in the waveguide-alike environment, MPCs are less resolvable. The contribution of noncoherent diffuse scattering to each cluster is more significant than in other cases. Consequently, $P_{\ell,\theta}$ and $P_{\ell,\phi}$ become less correlated due to severe distortions of the polarizations in such cases.

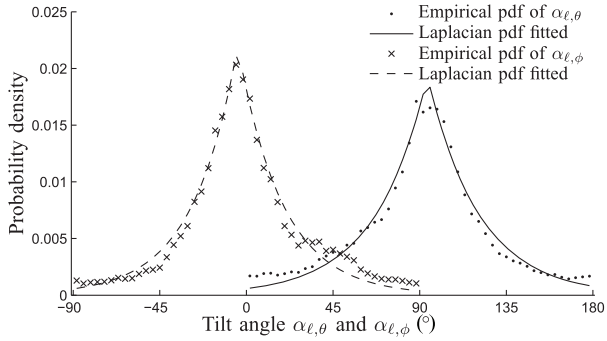

Fig. 5. Empirical pdfs and fitted Laplacian pdfs for tilt angle $\alpha_{\ell,\theta}$ and $\alpha_{\ell,\phi}$ in the scenario (a) OLoS corridor.

2) Statistics of the Tilt Angle $\alpha_{\ell,\theta}$ and $\alpha_{\ell,\phi}$: As discussed in Section II-B, the tilt angle α is referred to as the angle by which the semimajor axis of the titled ellipse rotates counterclockwise until being aligned with $\boldsymbol{e}_\theta$. Fig. 5 depicts for the scenario (a) the scatter plot of the empirical pdf of $\alpha_{\ell,\theta}$ and a truncated Laplacian pdf fitted to the pdf. The truncated Laplacian pdf is written as

$$f_{\mathrm{L}}(\alpha) = \frac{1}{2Bb}\exp\left\{-\frac{|\alpha-\mu|}{b}\right\} \tag{46}$$

where μ represents the mean of α, b is a scale parameter, and $B = \int_{\alpha_1}^{\alpha_2} \frac{1}{2b}\exp(-\frac{|\alpha-\mu|}{b})\mathrm{d}\alpha$ is a normalization factor. The consistency between the empirical pdf $f(\alpha_{\ell,\theta})$ and the truncated Laplacian pdf $f_{\mathrm{L}}(\alpha_{\ell,\theta})$ can also be observed for other scenarios. Table II reports the parameters of the fitted truncated Laplacian pdfs for five scenarios. From the table, we observed that the mean μ_{α_θ} of $\alpha_{\ell,\theta}$ is about 90° in the case of θ-polarization, and the mean μ_{α_ϕ} of $\alpha_{\ell,\phi}$ equals 0° in the case of ϕ-polarization. The scale parameters b are relatively large in laboratory and computer room scenarios for both $\alpha_{\ell,\theta}$ and $\alpha_{\ell,\phi}$. Since a larger b indicates a wider spread of tilt angle, this observation reveals that in the closed-areas such as laboratory and computer rooms, the tilt of the polarization ellipses is more diverse than in open areas such as a corridor and a hall. Furthermore, in the scenario (d) where the Rx is located in the computer room and the Tx is outside of the room, since the door of the computer room has been closed during the measurement, waves can also penetrate through the door or the wall in order to arrive at the Rx side. As a consequence, more MPCs are observed, which can be the reason for observing a larger spread for the tilt angle in this scenario. In addition, it can be observed from Table II that $\alpha_{\ell,\phi}$ has the scale parameter b_{α_ϕ} less than $\alpha_{\ell,\theta}$, indicating that the tilt angle of polarization ellipses is more concentrated when the transmitted waves are ϕ-polarized. Also, in laboratory and hall scenarios where human activities are involved, the scaling parameters for $\alpha_{\ell,\theta}$ are obviously larger than those for $\alpha_{\ell,\phi}$. Based on these observations, it is reasonable to speculate that tilt angle of θ-polarized ellipses can be influenced by human activities sensitively. Since the μ parameters of all considered propagation scenarios are approximately equal to 90° for θ-polarizations and 0° for ϕ-polarizations, the model can

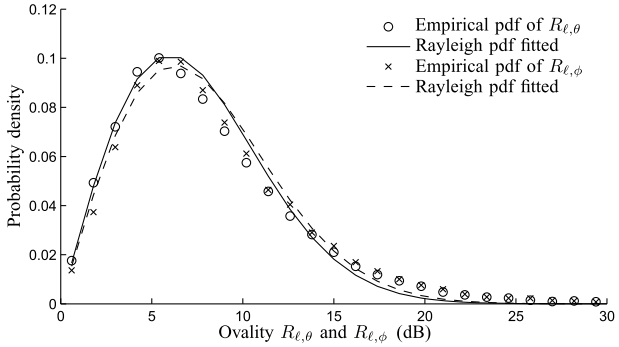

Fig. 6. Empirical pdfs and fitted Rayleigh pdfs for the ovality $R_{\ell,\theta}$ and $R_{\ell,\phi}$ in the scenario (a) OLoS corridor.

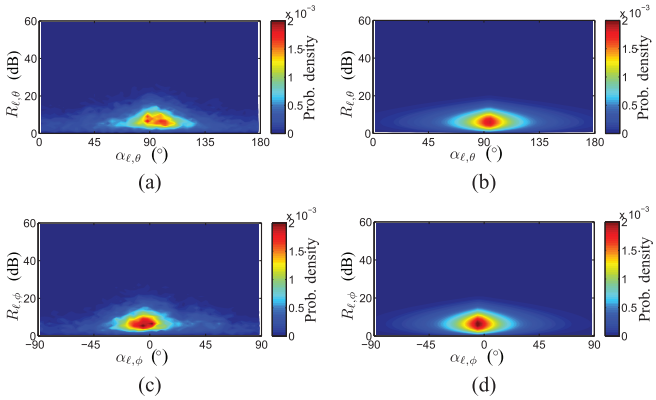

Fig. 7. (a) and (c) Emprical joint pdfs and (b) and (d) fitted pdfs for $\alpha_{\ell,\theta}$ and $R_{\ell,\theta}$, $\alpha_{\ell,\phi}$ and $R_{\ell,\phi}$, respectively, obtained in the scenario (a) of OLoS corridor.

be simplified to 90°-mean Laplacian distribution and 0°-mean Laplacian distribution for θ-polarizations and ϕ-polarizations, respectively.

3) Statistics of the Ovality Parameter $R_{\ell,\theta}$ and $R_{\ell,\phi}$: As discussed in Section II-B, the ovality parameters are nonnegative when being represented in decibel. Fig. 6 demonstrates an example of the empirical pdfs of $R_{\ell,\theta}$ and $R_{\ell,\phi}$ in the scenario (a). Both graphs exhibit the maxima around 9 dB for $R_{\ell,\theta}$ and $R_{\ell,\phi}$. The pdfs of Rayleigh distributions fit well to the scatter plots of empirical pdfs. The observation that the samples of $R_{\ell,\theta}$ and $R_{\ell,\phi}$ follow Rayleigh distributions is also obtained for other scenarios. Table II reports the scaling parameters ϱ_{R_θ} and ϱ_{R_ϕ} of the Rayleigh pdfs fitted to the empirical data for the five scenarios. It can be observed from Table II that the scaling parameter is slightly larger in the case of ϕ-polarization than θ-polarization, which implies that the average and standard deviation of ovality is more significant for waves transmitted with ϕ-polarization.[3] This is reasonable since in indoor scenarios, the θ-polarized wave may experience more obstacles than the ϕ-polarized wave especially in the case where a low-height ceiling has a complicated structure. Thus, the linear polarization is more easily retained for ϕ-polarized waves.

4) Joint PDFs of the Tilt Angle and the Ovality Parameter: Investigations are carried out on the correlation of the tilt angle and the ovality which are two parameters of the same ellipse. Fig. 7 illustrates examples of the empirical joint pdfs of $(\alpha_{\ell,\theta}, R_{\ell,\theta})$ and $(\alpha_{\ell,\phi}, R_{\ell,\phi})$, as well as the fitted bi-variate pdfs for the scenario (a). It can be observed from Fig. 7 that the empirical joint pdfs do not exhibit tilted shapes, indicating that no correlation exists between the values of $\alpha_{\ell,\theta}$ and $P_{\ell,\theta}$, and the same holds for $\alpha_{\ell,\phi}$ and $P_{\ell,\phi}$. Such observations are also obtained in the other scenarios.

5) Statistics of the Phase Difference $\Phi_{\ell,\theta}$ and $\Phi_{\ell,\phi}$: In the ellipse parameter vectors $\Phi_{\ell,\theta}$ and $\Phi_{\ell,\phi}$, the $\mathrm{sgn}(\Phi)$ indicates whether the elliptically polarized wave is left- or right-hand-oriented. Fig. 8(a) and (b) depicts, respectively, the empirical cumulative probability of $\Phi_{\ell,\theta}$ and $\Phi_{\ell,\phi}$ for the five scenarios. It is evident from Fig. 8(a) and (b) that $\Phi_{\ell,\theta}$ and $\Phi_{\ell,\phi}$ follow the uniform distribution within $[-\pi, \pi)$ which leads to the result

[3]For the samples following Rayleigh distributions, both the mean and the median values of the samples are proportional to the scaling parameter ϱ of the Rayleigh pdf, and the variance is proportional to ϱ^2.

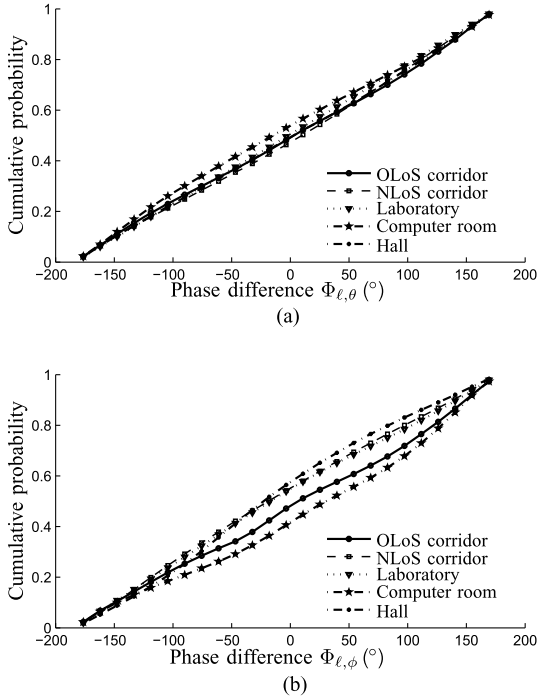

Fig. 8. Empirical cumulative probability distribution functions for (a) θ-TX-polarized waves and (b) ϕ-Tx polarized waves of $\Phi_{\ell,\theta}$ and $\Phi_{\ell,\phi}$ for five scenarios.

that the probabilities for $\mathrm{sgn}(\Phi)$ being positive and negative are identical in the considered scenarios.

It is worth mentioning that the proposed elliptical parameter model does not require the statistics of the exact values of phase differences $\Phi_{\ell,\theta}$ and $\Phi_{\ell,\phi}$. This is so because in the proposed model, any polarization ellipse can be obtained by rotating a standard ellipse with angle "α" anticlockwise. From (32) and (33) that describe the components $(E'_{\ell,\phi,\theta}, E'_{\ell,\theta,\theta})$ of a standard ellipse, we can see that the phase difference of a standard ellipse is always written as $\mathrm{sgn}(\Phi_{\ell,\theta})\frac{\pi}{2}$. It is natural that rotating the standard ellipse by "α" leads to a new phase difference for the resulting ellipse. However, this new phase difference can be indirectly calculated from the values of $R_{\ell,\theta}$, $\alpha_{\ell,\theta}$ and $\mathrm{sgn}(\Phi_{\ell,\theta})$. Therefore, considering this rationale, it is unnecessary to include the distribution of exact values of phase

differences $\Phi_{\ell,\theta}$ and $\Phi_{\ell,\phi}$ in the elliptical-parameter models. In other words, the statistical information of $\Phi_{\ell,\theta/\phi}$ has already been embedded in the models established for $R_{\ell,\theta/\phi}$, $\alpha_{\ell,\theta/\phi}$ and $\mathrm{sgn}(\Phi_{\ell,\theta/\phi})$.

6) Dependence Among the Parameters in $\boldsymbol{\vartheta}_{\ell,\theta}$ and $\boldsymbol{\vartheta}_{\ell,\phi}$: In the proposed stochastic polarization model, the polarization of a path is characterized by eight parameters of two polarization ellipses. It is necessary to check whether those parameters are correlated. If the correlation is significant, an empirical covariance matrix of them should be extracted based on measurements and included as part of the model. The measurement results show that the cross-correlation behavior among these parameters is different in the five scenarios considered. Table II lists the cross-correlation coefficient matrices of the elliptical parameters $\boldsymbol{\gamma}_\ell = [P_{\ell,\theta}, \alpha_{\ell,\theta}, R_{\ell,\theta}, \Phi_{\ell,\theta}, P_{\ell,\phi}, \alpha_{\ell,\phi}, R_{\ell,\phi}, \Phi_{\ell,\phi}]^{\mathrm{T}}$ for the five scenarios. It can be observed from Table II that in the scenario (a), the parameters in $\boldsymbol{\gamma}_\ell$ exhibit low cross-correlation coefficients in such a way that they can be considered to be uncorrelated, and for other scenarios, except for $P_{\ell,\theta}$ and $P_{\ell,\phi}$, the other parameters are also uncorrelated. From the results in five scenarios considered, we observed that the cross-correlation coefficient $\rho_{P_{\ell,\theta},P_{\ell,\phi}}$ between $P_{\ell,\theta}$ and $P_{\ell,\phi}$ varies from 0.11 to 0.69, whereas the cross-correlation among other ellipse parameters is usually less than 0.1. The scenarios where $\rho_{P_{\ell,\theta},P_{\ell,\phi}}$ is sorted in the descending order are the hall [i.e., the scenario (e), with $\rho_{P_{\ell,\theta},P_{\ell,\phi}} = 0.69$], the NLoS corridor [the scenario (b), with $\rho_{P_{\ell,\theta},P_{\ell,\phi}} = 0.63$], the laboratory (the scenario (c), with $\rho_{P_{\ell,\theta},P_{\ell,\phi}} = 0.44$), the computer room [the scenario (d), with $\rho_{P_{\ell,\theta},P_{\ell,\phi}} = 0.19$], and the OLoS corridor [the scenario (a), $\rho_{P_{\ell,\theta},P_{\ell,\phi}} = 0.11$]. Such a sequence is also consistent with the extent to which the pdf of $P_{\ell,\theta}$ and $P_{\ell,\phi}$ is tilted, as illustrated in Fig. 4. Based on these observations, it is necessary to define the cross-correlation between $P_{\ell,\theta}$ and $P_{\ell,\phi}$ depending on the type of indoor environments, and generate the random realizations of $P_{\ell,\theta}$ and $P_{\ell,\phi}$ by using their joint log-normal pdf with particular $\rho_{P_{\ell,\theta},P_{\ell,\phi}}$. The other parameters in $\boldsymbol{\gamma}$ may be generated independently by using the analytical pdfs consistent with the empirical samples in specific propagation scenarios.

IV. Model Validation

To understand the effect of applying the newly proposed ellipse-parameter-based modeling method, we select a propagation scenario, e.g., the scenario (a), and calculate the cumulative distribution functions (cdfs) of two performance indices, i.e., the capacities of dual-polarized MPCs, i.e., [3]

$$C = \log_2 \left[\det \left(I + \frac{\epsilon}{2} \boldsymbol{A}_\ell \boldsymbol{A}_\ell{}^H \right) \right]$$

where I is a 2×2 identity matrix and ϵ is the signal-to-noise ratio, and the singular value ratio of $\boldsymbol{A}_\ell$, i.e., [19]

$$\hat{\gamma}_\ell \doteq \hat{\varsigma}_{\ell,\min} / \hat{\varsigma}_{\ell,\max} \tag{47}$$

where $\hat{\varsigma}_{\ell,\min}$ and $\hat{\varsigma}_{\ell,\max}$ with $\hat{\varsigma}_{\ell,\min} \leq \hat{\varsigma}_{\ell,\max}$ represent the two singular values of $\boldsymbol{A}_\ell$. The singular values characterize the weighting factors of the effective two subchannels that arise when dual-polarized antenna arrays are used at both the Tx and the Rx.

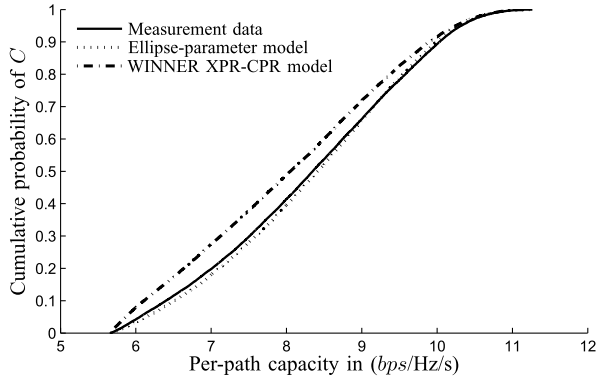

Fig. 9. CDFs of per-path capacity calculated based on empirical polarization matrices in the scenario (a), the matrix random realizations generated by using the proposed ellipse-parameter-based model and the WINNER XPR-CPR-based model that are established for the scenario (a).

For comparison purpose, the MPC polarization matrices $\boldsymbol{A}_\ell$ are obtained by using the following three approaches: 1) the empirical MPCs' polarization matrices estimated by using the ISI-SAGE algorithm; 2) the polarization matrix realizations generated by using the WINNER-defined XPR- and CPR-based model extracted from the empirical MPCs' polarization matrices; and 3) the polarization matrix realizations generated by using the ellipse-parameter-based model proposed in this study and extracted from the empirical matrix.

The procedure of generating random realizations of $\boldsymbol{A}_\ell$ based on the ellipse-parameter-based model consists of two steps. In the first step, the random pair of $(P_{\ell,\theta}, P_{\ell,\phi})$ is generated based on a bi-variate log-normal pdf, the random sets of α_θ and α_ϕ are generated from truncated Laplacian distributions, and the sets of R_θ and R_ϕ in decibels are obtained by using Rayleigh distributions. These distributions are extracted based on the empirical polarization matrices $\boldsymbol{A}_\ell$ of MPCs. In the second step, each element of $\boldsymbol{A}_\ell$ is calculated from (42)–(45) introduced in Section II-D with $\Phi^0_{\ell,\theta}, \Phi_{0,\phi}$ are randomly generated by using uniform distribution within $[-\pi, \pi)$, $\mathrm{sgn}(\Phi_{\ell,\theta})$, and $\mathrm{sgn}(\Phi_{\ell,\phi})$ are signs of the phase difference randomly selected from -1 and 1 with equal probability. For generating $\boldsymbol{A}_\ell$ based on the XPR and CPR parameters, we use the method similar with that proposed in [24], [25], [28], and [36], i.e., calculating directly from (5) with $\eta_{\ell,\theta}$ and $\eta_{\ell,\phi}$ and χ_ℓ generated randomly based on their empirical pdfs extracted from the MPCs' polarization matrices.

Figs. 9 and 10 illustrate, respectively, the cdfs of channel capacity and of $\hat{\gamma}_\ell$ estimated by using $\boldsymbol{A}_\ell$ generated by using the aforementioned three methods with the SNR fixed to be 20 dB. It can be observed from both figures that compared with the WINNER XPR-CPR-based modeling method, the cdf graph generated by using the newly proposed ellipse-parameter-based modeling method is more tightly aligned with the empirical cdf graph. More specifically, from Fig. 9, it can be observed that the maximum distance between the empirical capacity cumulative

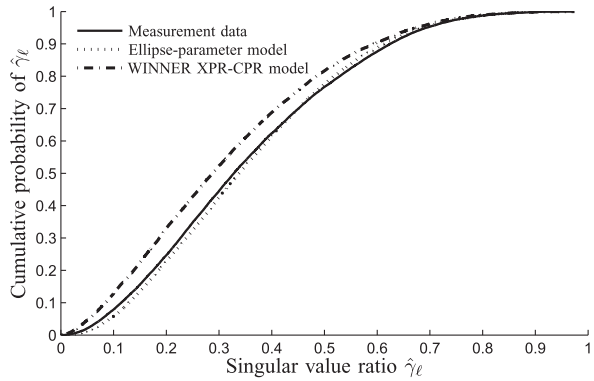

Fig. 10. CDFs of singular value ratio $\hat{\gamma}_\ell$ calculated based on empirical polarization matrices in the scenario (a), the matrix random realizations generated by using the proposed ellipse-parameter-based model and the WINNER XPR-CPR-based model that are established for the scenario (a).

probability and that calculated by using the WINNER XPR-CPR-based model is 10%, which is reduced to 1% when the newly proposed model is used. Similar improvement by using the new model can also be observed for the polarization matrix singular value ratio. These observations demonstrate that the proposed modeling method is superior to the WINNER XPR- and CPR-based modeling approach when being applied to reproduce the statistical properties of MPC polarization status. Besides the aforementioned approaches, model evaluation can be also conducted from other aspects where the conventional model may be inapplicable. For example, we can also calculate analytically the statistics of correlations among the entries of $\boldsymbol{A}_\ell$ by using (42)–(45) together with the extracted distributions of the elliptical parameters, and check the consistency with real data. Such calculations are difficult to carry out with the conventional XPR- and CPR-based models.

It can be observed from Table II that the proposed elliptical-parametric polarization model requires totally 11 parameters to specify the pdfs required,[4] while in the WINNER-defined XPR and CPR-based model, only six parameters are used to specify the pdfs of the XPRs and CPR given the magnitude of a_ℓ [24]. It is natural that with a larger number of parameters, model fitting can be performed with a higher accuracy. However, when the resultant model applies to the cases that are different from those considered for model construction, the prediction accuracy may be worse for models with a larger number of parameters than less parameters. This is reasonable because as the number of parameters increases, the difficulty in tuning the established model to fit the new data increases, leading to larger estimation errors eventually. To prevent such problems, it is necessary to categorize the propagation scenarios with more refined definitions, and conduct extensive measurements for capturing channel characteristics of ergodicity to enhance the model's applicability in desired scenarios.

[4]Five of the eleven parameters specify the 2-D Gaussian pdf for $P_{\ell,\theta}$ and $P_{\ell,\phi}$, four for the truncated Laplacian pdfs of the tilt angles $\alpha_{\ell,\theta}$ and $\alpha_{\ell,\phi}$, respectively, and two for the Rayleigh pdfs of the ovality parameters $R_{\ell,\theta}$ and $R_{\ell,\phi}$, respectively.

V. Conclusion

The conventional GSCMs constructed from real measurements neglect some stochastic properties of polarization matrices of individual propagation paths. In this contribution, a geometrical modeling approach has been proposed for characterizing the stochastic behaviors of 2×2 polarization matrices of MPCs. The columns of a polarization matrix are represented by two ellipses, each uniquely determined by its ovality, tilt angle, right- or left-hand-rotating orientation, and the ellipse size. The resulting stochastic polarization model consists of the pdfs of these parameters extracted from empirical data. Measurements collected in indoor environments have been applied to extract the models using the proposed method. Results have shown that the sizes of two polarization ellipses of one path can be described as correlated log-normal random variables. The distributions of the tilt angle follow truncated Laplacian pdfs, and the ovality parameter represented in dB follows Rayleigh distributions. The ellipses were found to have equal probability for being left- and right-hand rotating. Finally, except for the sizes of the ellipses, the other parameters of the two ellipses for one path were uncorrelated. Compared with the conventional GSCM XPR- and CPR-based models, the proposed polarization model performs better at simulating the distributions of per-path capacities and singular value ratio of polarization matrix. The models established can be complementary to the existing GSCMs for achieving a better consistency of simulated channel properties with the real channels particularly in the aspects of polarizations.

Appendix
Derivations of (19)–(21)

A general form of a polarization ellipse in (15) can be rewritten after simple manipulations as

$$\xi_{\ell,1,\theta} E^2_{\ell,\theta,\theta}(t) + \xi_{\ell,3,\theta} E^2_{\ell,\phi,\theta}(t) - \xi_{\ell,2,\theta} E_{\ell,\theta,\theta}(t) E_{\ell,\phi,\theta}(t) = 1 \tag{48}$$

with

$$\xi_{\ell,1,\theta} = \frac{1}{\boldsymbol{E}^2_{\ell,\theta,\theta,\max} \sin^2 \Phi_{\ell,\theta}} \tag{49}$$

$$\xi_{\ell,2,\theta} = \frac{2\cos\Phi_{\ell,\theta}}{\boldsymbol{E}_{\ell,\theta,\theta,\max} \boldsymbol{E}_{\ell,\phi,\theta,\max} \sin^2 \Phi_{\ell,\theta}} \tag{50}$$

$$\xi_{\ell,3,\theta} = \frac{1}{\boldsymbol{E}^2_{\ell,\phi,\theta,\max} \sin^2 \Phi_{\ell,\theta}}. \tag{51}$$

Dividing both sides of (48) by $E_{\ell,\theta,\theta}(t) \cdot E_{\ell,\phi,\theta}(t)$, and introducing

$$x(t) = \frac{E_{\ell,\theta,\theta}(t)}{E_{\ell,\phi,\theta}(t)} \tag{52}$$

in (48) yields

$$\xi_{\ell,1,\theta} x(t) + \xi_{\ell,3,\theta} \frac{1}{x(t)} - \xi_{\ell,2,\theta} = \frac{1}{x(t)} \frac{1}{E^2_{\ell,\phi,\theta}(t)}$$
$$\Rightarrow E^2_{\ell,\phi,\theta}(t) = \frac{1}{\xi_{\ell,1,\theta} x(t)^2 + \xi_{\ell,3,\theta} - \xi_{\ell,2,\theta} x(t)}. \tag{53}$$

It can be shown that the length r_ℓ of vector $\boldsymbol{E}_{\ell,\theta}(t)$ introduced in (9) can be calculated as a function of $x(t)$

$$r_\ell\left(x(t)\right) = \left|\boldsymbol{E}_{\ell,\theta}(t)\right| = \sqrt{\frac{1+x(t)^2}{\xi_{\ell,1,\theta}x(t)^2+\xi_{\ell,3,\theta}-\xi_{\ell,2,\theta}x(t)}}. \tag{54}$$

For notational simplicity, $x(t)$ is written as x in the following. Since the trajectory of vector $\boldsymbol{E}_{\ell,\theta}(t)$ is an ellipse, $r_\ell(x)$ achieves its maximum and minimum when $E_{\ell,\phi,\theta}(t)$ and $E_{\ell,\theta,\theta}(t)$ coincide with the ellipse's semimajor and semi-minor axes, respectively. Thus, by equating $\mathrm{d}r_\ell/\mathrm{d}x$ with 0, the angles between the semimajor and semiminor axes and the horizontal axis can be calculated as

$$\begin{aligned}
&\frac{\mathrm{d}r_\ell}{\mathrm{d}x} = 0\\
&\Rightarrow \frac{-\xi_{\ell,2,\theta}x^2+2\left(\xi_{\ell,1,\theta}-\xi_{\ell,3,\theta}\right)x+\xi_{\ell,2,\theta}}{2\sqrt{\frac{1+x^2}{\xi_{\ell,1,\theta}x^2+\xi_{\ell,3,\theta}-\xi_{\ell,2,\theta}x}}\left(\xi_{\ell,1,\theta}x^2+\xi_{\ell,3,\theta}-\xi_{\ell,2,\theta}x\right)^2} = 0\\
&\Rightarrow x^2 - 2\frac{\left(\xi_{\ell,1,\theta}-\xi_{\ell,3,\theta}\right)x}{\xi_{\ell,2,\theta}} - 1 = 0.
\end{aligned} \tag{55}$$

Substituting x in (55) by $x=\tan\varphi$ with φ being the angle of $\boldsymbol{E}_{\ell,\theta}(t)$ and multiplying both sides of (55) with $\cos^2\varphi$, it can be shown after trigonometric duplication operations that (55) can be written as

$$\tan 2\varphi = \frac{-\xi_{\ell,2,\theta}}{\left(\xi_{\ell,1,\theta}-\xi_{\ell,3,\theta}\right)} \tag{56}$$

$$= \frac{2E_{\ell,\theta,\theta,\max}E_{\ell,\phi,\theta,\max}\cos\Phi_{\ell,\theta}}{E^2_{\ell,\phi,\theta,\max}-E^2_{\ell,\theta,\theta,\max}}. \tag{57}$$

To satisfy the equality in (57), φ may have two values, i.e., $\varphi_{\ell,1,\theta}$ and $\varphi_{\ell,2,\theta}$, calculated as, respectively,

$$\varphi_{\ell,1,\theta} = \frac{1}{2}\tan^{-1}\left(\frac{2E_{\ell,\theta,\theta,\max}E_{\ell,\phi,\theta,\max}\cos\Phi_{\ell,\theta}}{E^2_{\ell,\phi,\theta,\max}-E^2_{\ell,\theta,\theta,\max}}\right) \tag{58}$$

$$\varphi_{\ell,2,\theta} = \varphi_{\ell,1,\theta}+\frac{\pi}{2}. \tag{59}$$

The tilt angle $\alpha_{\ell,\theta}$, defined to be the angle between $\boldsymbol{e}_\phi$ and the semimajor axis of the ellipse, equals either $\varphi_{\ell,1,\theta}$ or $\varphi_{\ell,2,\theta}$, depending on whether $r\left(\tan(\varphi_{\ell,i,\theta})\right), i\in\{1,2\}$ equals the length of the semimajor axis. Based on this result, (19) and (20) are obtained.

REFERENCES

[1] S. Mukherjee, *WiMAX Antennas Primer—A Guide to MIMO and Beamforming*, [Online]. Available: http://mmwave.com/about/wimax-page/wimax-antennas-primer-guide-mimo-beamforming/, 2010.

[2] F. Borko and A. A. Syed, *Long Term Evolution: 3GPP LTE Radio and Cellular Technology*. New York, NY, USA: Taylor & Francis, Apr. 2009.

[3] G. J. Foschini and M. J. Gans, "On limits of wireless communications in a fading environment when using multiple antennas," *Wireless Pers. Commun.*, vol. 6, no. 3, pp. 311–335, 1998.

[4] M. Andrews, P. Mitra, and R. deCarvalho., "Tripling the capacity of wireless communications using electromagnetic polarization," *Lett. Nat.*, vol. 409, pp. 316–318, 2001.

[5] P. Kyritsi, D. Cox, R. Valenzuela, and P. Wolniansky, "Effect of antenna polarization on the capacity of a multiple element system in an indoor environment," *IEEE J. Sel. Areas Commun.*, vol. 20, no. 6, pp. 1227–1239, Aug. 2002.

[6] L. Lukama, K. Konstantinou, and D. Edwards, "Three-branch orthogonal polarisation diversity," *Electron. Lett.*, vol. 37, no. 20, pp. 1258–1259, 2001.

[7] C. B. Dietrich Jr., K. Dietze, J. Nealy, W. Stutzman, "Spatial, polarization, and pattern diversity for wireless handheld terminals," *IEEE Trans. Antennas Propag.*, vol. 49, no. 9, pp. 1271–1281, Sep. 2001.

[8] G. Gupta, B. Hughes, and G. Lazzi, "On the degrees of freedom in linear array systems with tri-polarized antennas," *IEEE Trans. Wireless Commun.*, vol. 7, no. 7, pp. 2458–2462, Jul. 2008.

[9] H. Jian and J. Liu, "Application study of dual-polarization smart antenna in TD-SCDMA system," in *Proc. Int. Conf. Meas. Technol. Mechatron. Autom. (ICMTMA'10)*, 2010, pp. 679–682.

[10] L. Yuan, P. Mugen, and J. Jiang, "Investigation of dual-polarization antenna scheme in TD-LTE systems," in *Proc. IEEE Int. Conf. Wireless Inf. Technol. Syst. (ICWITS'12)*, 2012, pp. 1–4.

[11] F. Wang, X. Cheng, X. Yin, and B. Jiao, "Capacity comparison between dual-polarized antenna system and omnidirectional antenna system in 3-D propagation environments," in *Proc. IEEE Globe Commun. Conf. (GLOBECOM'13)*, Dec. 2013, pp. 4263–4268.

[12] M. Mtumbuka and D. Edwards, "Performance of MIMO systems employing co-located orthogonally polarized antennas in micro-cellular environments," in *Proc. IEEE 16th Int. Symp. Pers. Indoor Mobile Radio Commun. (PIMRC'05)*, 2005, pp. 609–613.

[13] D. Yu, A. Burr, and G. White, "Performance of MIMO systems with combined polarization multiplexing and transmit diversity," in *Proc. IEEE 61st Veh. Technol. Conf. (VTC'05 Spring)*, 2005, vol. 2, pp. 869–873.

[14] N. Das, T. Inoue, T. Taniguchi, and Y. Karasawa, "An experiment on MIMO system having three orthogonal polarization diversity branches in multipath-rich environment," in *Proc. IEEE 60th Veh. Technol. Conf. (VTC'04 Fall)*, 2004, vol. 2, pp. 1528–1532.

[15] C. Oestges, B. Clerckx, M. Guillaud, and M. Debbah, "Dual-polarized wireless communications: From propagation models to system performance evaluation," *IEEE Trans. Wireless Commun.*, vol. 7, no. 10, pp. 4019–4031, Oct. 2008.

[16] F. Quitin, C. Oestges, F. Horlin, and P. De Doncker, "Multipolarized MIMO channel characteristics: Analytical study and experimental results," *IEEE Trans. Antennas Propag.*, vol. 57, no. 9, pp. 2739–2745, Sep. 2009.

[17] A. Panahandeh, F. Quitin, J. Dricot, F. Horlin, C. Oestges, and P. De Doncker, "A time-variant statistical model for the polarization of received electromagnetic waves in indoor communication channels," in *Proc. Int. Conf. Comput. Netw. Commun. (ICNC'12)*, 2012, pp. 262–266.

[18] B. Fleury, X. Yin, P. Jourdan, and A. Stucki, "High-resolution channel parameter estimation for communication systems equipped with antenna arrays (invited paper)," in *Proc. 13th IFAC Symp. Syst. Ident. (SYSID'03)*, 2003.

[19] X. Yin, B. Fleury, P. Jourdan, and A. Stucki, "Polarization estimation of individual propagation paths using the sage algorithm," in *14th IEEE Proc. Pers. Indoor Mobile Radio Commun. (PIMRC'03)*, Sep. 2003, vol. 2, pp. 1795–1799.

[20] F. Quitin *et al.*, "A time-variant statistical channel model for tri-polarized antenna systems," in *Proc. IEEE 21st Int. Symp. Pers. Indoor Mobile Radio Commun. (PIMRC'10)*, 2010, pp. 64–69.

[21] F. Quitin, C. Oestges, F. Horlin, and P. De Doncker, "Polarimetric measurements for spatial wideband MIMO channels," in *Proc. IEEE 69th Veh. Technol. Conf. (VTC'09 Spring)*, 2009, pp. 1–5.

[22] F. Quitin, C. Oestges, F. Horlin, and P. De Doncker, "Polarization measurements and modeling in indoor NLOS environments," *IEEE Trans. Wireless Commun.*, vol. 9, no. 1, pp. 21–25, Jan. 2010.

[23] *Spatial Channel Model for Multiple Input Multiple Output (MIMO) Simulations (Release 7)*, 3GPP TR25.996 V7.0.0 Standard, 2007.

[24] *WINNER II Channel Models*, IST-WINNER II Deliverable 1.1.2 v.1.2. Standard, 2007 [Online]. Available: http://www.ist-winner.corg/deliverables.html

[25] M. Shafi *et al.*, "Polarized MIMO channels in 3-D: Models, measurements and mutual information," *IEEE J. Sel. Areas Commun.*, vol. 24, no. 3, pp. 514–527, Mar. 2006.

[26] ITU (International Telecommunication Union). "Guidelines for evaluation of radio interface technologies for IMT-advanced," Tech. Rep. ITU-R M.2135, 2007.

[27] F. Quitin, C. Oestges, F. Horlin, and P. De Doncker, "Clustered channel characterization for indoor polarized MIMO systems," in *Proc. 20th Int. Symp. Pers. Indoor Mobile Radio Commun. (PIMRC'09)*, 2009, pp. 1064–1068.
[28] F. Quitin, C. Oestges, F. Horlin, and P. De Doncker, "A polarized clustered channel model for indoor multiantenna systems at 3.6 Ghz," *IEEE Trans. Veh. Technol.*, vol. 59, no. 8, pp. 3685–3693, Oct. 2010.
[29] S. Jaeckel, K. Borner, L. Thiele, and V. Jungnickel, "A geometric polarization rotation model for the 3-D spatial channel model," *IEEE Trans. Antennas Propag.*, vol. 60, no. 12, pp. 5966–5977, Dec. 2012.
[30] T. Imai and K. Kitao, "Polarization dispersion characteristics of propagation paths in urban mobile communication environment," in *Proc. IEEE Veh. Technol. Conf. (VTC'11 Fall)*, 2011, pp. 1–5.
[31] *Elektrobit PropSim Homepage* [Online]. Available: http://www.propsim.com/
[32] M. Steinbauer, A. Molisch, and E. Bonek, "The double-directional radio channel," *IEEE Antennas Propag. Mag.*, vol. 43, no. 4, pp. 51–63, Aug. 2001.
[33] B. H. Fleury, P. Jourdan, and A. Stucki, "High-resolution channel parameter estimation for MIMO applications using the SAGE algorithm," in *Proc. Int. Zurich Semin. Broadband Commun.*, Zurich, Switzerland, Feb. 2002, vol. 30, pp. 1–9.
[34] X. Yin, B. Fleury, P. Jourdan, and A. Stucki, "Polarization estimation of individual propagation paths using the Sage algorithm," in *Proc. IEEE 14th Pers. Indoor Mobile Radio Commun. (PIMRC'03)*, 2003, vol. 2, pp. 1795–1799.
[35] R. C. Jones, "A new calculus for the treatment of optical systems," *J. Opt. Soc. Amer.*, vol. 31, no. 7, pp. 488–493, 1941.
[36] V. Eiceg, H. Sampath, and S. Catreux-Erceg, "Dual-polarization versus single-polarization MIMO channel measurement results and modeling," *IEEE Trans. Wireless Commun.*, vol. 5, no. 1, pp. 28–33, Jan. 2006.
[37] R. R. G. Yang, *Electromagnetic Fields and Waves*, 2nd ed. China: Higher Education Press, Jan. 1, 2013.
[38] N. Czink, "The random-cluster model—A stochastic MIMO channel model for broadband wireless communication systems of the 3rd generation and beyond," Ph.D. dissertation, Dept. Electron. Inf. Technologies, Technol. Univ. Vienna, Wien, Austria, Dec. 2007.
[39] H. Akaike, "A new look at the statistical model identification," *IEEE Trans. Automat. Control*, vol. 19, no. 6, pp. 716–723, Dec. 1974.
[40] C.-L. Ho, "Calculating the mean and variance of power sums with two log-normal components," *IEEE Trans. Veh. Technol.*, vol. 44, no. 4, pp. 756–762, Nov. 1995.
[41] N. Mehta, J. Wu, A. Molisch, and J. Zhang, "Approximating a sum of random variables with a lognormal," *IEEE Trans. Wireless Commun.*, vol. 6, no. 7, pp. 2690–2699, Jul. 2007.

Xuefeng Yin (S'01–M'06) received the Ph.D. degree in wireless communications from Aalborg University, Aalborg, Denmark, in 2006.

From 2006 to 2008, he worked as an Assistant Professor with Aalborg University. In 2008, he joined as an Associate Professor with the College of Electronics and Information Engineering, Tongji University, Shanghai, China. He has authored more than 60 technical papers, co-authored a book on channel characterization and modelling, and holds more than 10 PCT-patents as the first inventor. His research interests include high-resolution parameter estimation for propagation channels, channel characterization and stochastic modelling for 5G wireless communications, radar signal processing, and target recognition.

Dr. Yin has served as Symposium Chair and Member of the technical program committee for some international conferences, and Reviewer for a number of international journals including the IEEE TRANSACTIONS ON VEHICULAR TECHNOLOGY, the IEEE TRANSACTIONS ON SIGNAL PROCESSING, and the IEEE TRANSACTIONS ON ANTENNA AND PROPAGATION.

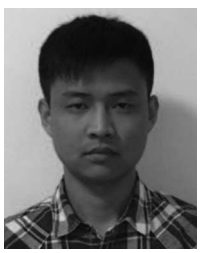

Yongyu He (S'14) was born in Ping'an, China, in 1989. He received the Bachelor's degree in electronics science and technology and the Master's degree in circuit and systems from the Tongji University, Shanghai, China, in July 2011 and April 2014, respectively. He is currently pursuing the Doctor degree in physics at the same university.

His research interests include wireless propagation channel and more specifically, the characterization and modeling of millimeter-wave and higher frequency band channels, and self-interference channels.

Cen Ling (S'14) was born in Suzhou, China, in 1990. She received the Bachelor's degree in electronic science and technology from Nanjing University of Posts and Telecommunication, Nanjing, China, in July 2012.

In September 2009, she started the Ph.D. program in control science and engineering at Tongji University, Shanghai, China. From February to July 2014, she was a Visiting Ph.D. Student at the Polytechnic University of Catalonia, Barcelona, Spain. Her research interests include channel parameter estimation and modeling, cooperative communication, and network optimization.

Li Tian (S'12–M'15) was born in Xiantao, China, in 1988. He received the Bachelor's degree in communication engineering and the Ph.D. degree in control science and control engineering from Tongji University, Shanghai, China, in July 2009 and January 2015, respectively.

From 2013 to 2014, he was a Visiting Ph.D Student at the Department of Electronics and Information Systems (DEIS), University of Bologna, Bologna, Italy, working with Prof. Vittorio Degli-Esposti. He participated in the 5G project sponsored by National Natural Science Foundation of China. He is currently a Senior Engineer with the Department of Algorithms, ZTE Corporation, Shangai, China. His research interests include 5G channel modeling and new air-interface.

Dr. Tian serves as Reviewer for a number of international journals including the IEEE TRANSACTIONS ON VEHICULAR TECHNOLOGY, the IEEE ANTENNAS AND WIRELESS PROPAGATION LETTERS, and *International Journal of Antennas and Propagation*.

Xiang Cheng (S'05–M'10–SM'13) received the Ph.D. degree from Heriot-Watt University, Edinburgh, U.K., and the University of Edinburgh, Edinburgh, U.K., in 2009, where he received the Postgraduate Research Thesis Prize.

He has been with Peking University, Bejing, China, since 2010, first as a Lecturer, and then as an Associate Professor since 2012. He has authored more than 100 research papers in journals and conference proceedings. His research interests include mobile propagation channel modeling and simulation, next-generation mobile cellular systems, intelligent transportation systems, and hardware prototype development.

Dr. Cheng has served as Symposium Leading-Chair, Co-Chair, and a Member of the Technical Program Committee for several international conferences. He was the recipient of several best paper awards in the IEEE International Conference on ITS Telecommunications (ITST 2012), the IEEE International Conference on Communications in China (ICCC 2013), and the 17th International IEEE Conference on Intelligent Transportation Systems (ITSC 2014). He was also the recipient of the "2009 Chinese National Award for Outstanding Overseas Ph.D. Student" for his academic excellence and outstanding performance.